JOURNAL OF PETROLOGY | VOLUME 49 | NUMBER 6 | PAGES 1043–1068 | 2008 | doi:10.1093/petrology/egn017

Igneous Layering, Fractional Crystallization and Growth of Granitic Plutons: the Dolbel Batholith in SW Niger

E. PUPIER[1], P. BARBEY[1]*, M. J. TOPLIS[2] AND F. BUSSY[3]

[1]CRPG, NANCY UNIVERSITÉ, CNRS, B.P. 20, 54501 VANDŒUVRE LÈS NANCY CEDEX, FRANCE

[2]DTP, OBSERVATOIRE MIDI-PYRÉNÉES, 14 AVENUE EDOUARD BELIN, 31400 TOULOUSE, FRANCE

[3]INSTITUTE OF MINERALOGY AND GEOCHEMISTRY, ANTHROPOLE, UNIVERSITY OF LAUSANNE, CH-1015 LAUSANNE, SWITZERLAND

RECEIVED OCTOBER 2, 2007; ACCEPTED MARCH 10, 2008
ADVANCE ACCESS PUBLICATION APRIL 19, 2008

This study reassesses the development of compositional layering during the growth of granitic plutons, with emphasis on fractional crystallization and its interaction with both injection and inflation-related deformation. The Dolbel batholith (SW Niger) consists of 14, kilometre-sized plutons emplaced by pulsed magma inputs. Each pluton has a coarse-grained core and a peripheral layered series. Rocks consist of albite ($An_{\leq 11}$), K-feldspar (Or_{96-99}, Ab_{1-4}), quartz, edenite ($X_{Mg} = 0{\cdot}37–0{\cdot}55$), augite ($X_{Mg} = 0{\cdot}65–0{\cdot}72$) and accessories (apatite, titanite and Fe–Ti-oxides). Whole-rock compositions are metaluminous, sodic ($K_2O/Na_2O = 0{\cdot}49–0{\cdot}62$) and iron-rich [$FeO_{tot}/(FeO_{tot} + MgO) = 0{\cdot}65–0{\cdot}82$]. The layering is present as size-graded and modally graded, sub-vertical, rhythmic units. Each unit is composed of three layers, which are, towards the interior: edenite ± plagioclase ($C_{a/p}$), edenite + plagioclase + augite + quartz (C_q), and edenite + plagioclase + augite + quartz + K-feldspar (C_k). All phases except quartz show zoned microstructures consisting of external intercumulus overgrowths, a central section showing oscillatory zoning and, in the case of amphibole and titanite, complexly zoned cores. Ba and Sr contents of feldspars decrease towards the rims. Plagioclase crystal size distributions are similar in all units, suggesting that each unit experienced a similar thermal history. Edenite, characteristic of the basal $C_{a/p}$ layer, is the earliest phase to crystallize. Microtextures and phase diagrams suggest that edenite cores may have been brought up with magma batches at the site of emplacement and mechanically segregated along the crystallized wall, whereas outer zones of the same crystals formed in situ. *The subsequent C_q layers correspond to cotectic compositions in the Qz–Ab–Or phase diagram at $P_{H2O} = 5$ kbar. Each rhythmic unit may therefore correspond to a magma batch and their repetition to crystallization of recurrent magma recharges. Microtextures and chemical variations in major phases allow four main crystallization stages to be distinguished: (1) open-system crystallization in a stirred magma during magma emplacement, involving dissolution and overgrowth (core of edenite and titanite crystals); (2)* in situ *fractional crystallization in boundary layers ($C_{a/p}$ and C_q layers); (3) equilibrium 'en masse' eutectic crystallization (C_k layers); (4) compaction and crystallization of the interstitial liquid in a highly crystallized mush (e.g. feldspar intercumulus overgrowths). It is concluded that the formation of the layered series in the Dolbel plutons corresponds principally to* in situ *differentiation of successive magma batches. The variable thickness of the C_k layers and the microtextures show that crystallization of a rhythmic unit stops and it is compacted when a new magma batch is injected into the chamber. Therefore, assembly of pulsed magma injections and fractional crystallization are independent, but complementary, processes during pluton construction.*

KEY WORDS: *layered igneous rocks; granite; pluton; magma chamber; fractional crystallization*

INTRODUCTION

Formation of plutons is currently considered to be the result of incremental growth by pulsed injections of silicic or mafic magmas, over various periods of time (e.g. Aranguren *et al.*, 1997; McNulty *et al.*, 2000; Petford *et al.*, 2000; Coleman *et al.*, 2004; among a wealth of publications). Nevertheless, simple assembly of magma pulses is not sufficient for understanding the petrological and

*Corresponding author. Telephone: 33 3 83 59 42 34. Fax: 33 3 83 51 17 98. E-mail: barbey@crpg.cnrs-nancy.fr

structural characteristics of granitic plutons (Spera & Bohrson, 2001; Pons *et al.*, 2006), and consideration of additional processes is required. Although many processes have been proposed to occur in magma chambers during the formation of granitic plutons (Barrière, 1981; Parsons & Becker, 1987; Tobisch *et al.*, 1997; Hodson, 1998; Wiebe & Collins, 1998; Wiebe *et al.*, 2002; Pons *et al.* 2006), their exact role and relative importance remain open to debate as illustrated, for example, by contrasting opinions concerning the origin of the Tuolumne Batholith in central Sierra Nevada (Glazner *et al.*, 2004; Zak & Paterson, 2005). The aim of the present study is to reassess the role of processes that occur in magma chambers during the formation of granitic plutons, with emphasis on the role of fractional crystallization in boundary layers (i.e. in temperature and compositional gradients) and its interplay with new magma injection and inflation-related deformation during pluton growth and solidification.

Even though the physical properties of basaltic and granitic magmas are different, the study of mafic igneous complexes provides insight into the magmatic processes occurring during the construction of magma chambers in the crust. For example, compositionally zoned minerals in cumulate rocks are commonly interpreted in terms of the degree of local melt differentiation, and such chemical gradients can be used to constrain liquid evolution and residence times (e.g. Maaløe, 1976; Tegner, 1997; Markl & White, 1999; Zellmer *et al.*, 1999; Jang & Naslund, 2001; Boyce & Hervig, 2008; Toplis et al., 2008). Similarly, unzoned crystals typical of adcumulate textures are interpreted to be the result of small-scale convection in liquids or diffusion, leading to the progressive removal of interstitial porosity with little or no mineralogical and compositional variation relative to the cumulus assemblage (e.g. Morse, 1980; Hunter, 1987; Tait & Jaupart, 1996). At longer length scales, modally graded layered sequences and 'turbidite-like' structures have been related to fractional crystallization in boundary layers, and to crystal sorting and accumulation through density currents and large-scale convection (e.g. Wager & Brown, 1968; Morse, 1980; Parsons, 1987; Cawthorn, 1996; Irvine *et al.*, 1998).

Returning to the case of more silicic and alkaline magmatic rocks, noteworthy examples of igneous layering are well known in syenite and granite plutons, with rhythmic units, mineral grading, cross-stratification and trough layering (Wager & Brown, 1968; Barrière, 1981; Parsons, 1987; Parsons & Becker, 1987; Cawthorn, 1996; Tobisch *et al.*, 1997; Hodson, 1998). These structures suggest that hydrodynamic sorting and thermal convection are also likely to occur in granitic plutons, at least at the scale of a single magmatic unit (Wiebe & Collins, 1998; Weinberg *et al.*, 2001; Wiebe *et al.*, 2002; Pons *et al.*, 2006). Furthermore, recent experimental and numerical studies have shown that the viscosities of silicic magmas cluster around $10^{4\cdot5}$ Pa s, and do not change significantly, as long as the crystal fraction remains below 30–50% (Scaillet *et al.*, 1996, 1997, 1998; Clemens & Petford, 1999). These viscosity values are lower than formerly considered; thus it would appear that viscosity is not an obstacle to convection in silicic magma chambers (even though length and time scales are likely to be different from those encountered in mafic chambers), nor should it impede small scale crystal–melt segregation. Therefore, the study of igneous layering in granitic bodies may provide us with information on the role of magma chamber processes—especially fractional crystallization in boundary layers—during the construction of granitic plutons.

The assessment of the role of crystallization in a thermal boundary layer requires careful choice of rock samples. For example: (1) layering formed by crystal settling and hydrodynamic sorting should be avoided as much as possible, and this restricts sampling to near-vertical layering close to the walls of plutons; (2) deformation gradients related to pluton inflation need to be moderate for the igneous textures to be preserved; (3) bulk compositions should be close to experimentally determined phase diagrams to have an appropriate reference frame; (4) mineral phases should display chemical zoning, allowing the extent of melt differentiation to be assessed. In the light of these constraints, the Dolbel batholith in SW Niger has been selected for this study, as it fulfils all of the above criteria. After a presentation of the plutons and their structural features, we describe the microtextures and compositions of the main mineral phases and then discuss the development of the compositional layering during the course of pluton growth, with particular emphasis on fractional crystallization in boundary layers.

GEOLOGICAL SETTING

The Dolbel batholith (Liptako province, SW Niger; Machens, 1967; Pons *et al.*, 1995) is located in the northeastern part of the Leo Rise (Fig. 1a), an extensive 2·1 Ga granite–greenstone terrane considered to be a major zone of crustal growth (Milési *et al.*, 1989; Abouchami *et al.*, 1990; Boher *et al.*, 1992). The batholith consists of 14, kilometre-sized, plutons forming a narrow NW–SE-trending belt, perpendicular to the regional strike of the surrounding greenstones (Fig. 1b). The shape of the plutons, deflection of the country-rock schistosity and crosscutting relationships show that plutons were emplaced syntectonically, in a northward-trending succession (γ^1 to γ^{14}). The small size of the plutons and their distribution along a NW–SE linear array parallel to the direction of regional shortening were considered by Pons *et al.* (1995) to result from pulsed magma ascent and ponding, controlled by regional deformation that created a series of large tension gashes parallel to the σ_1 direction.

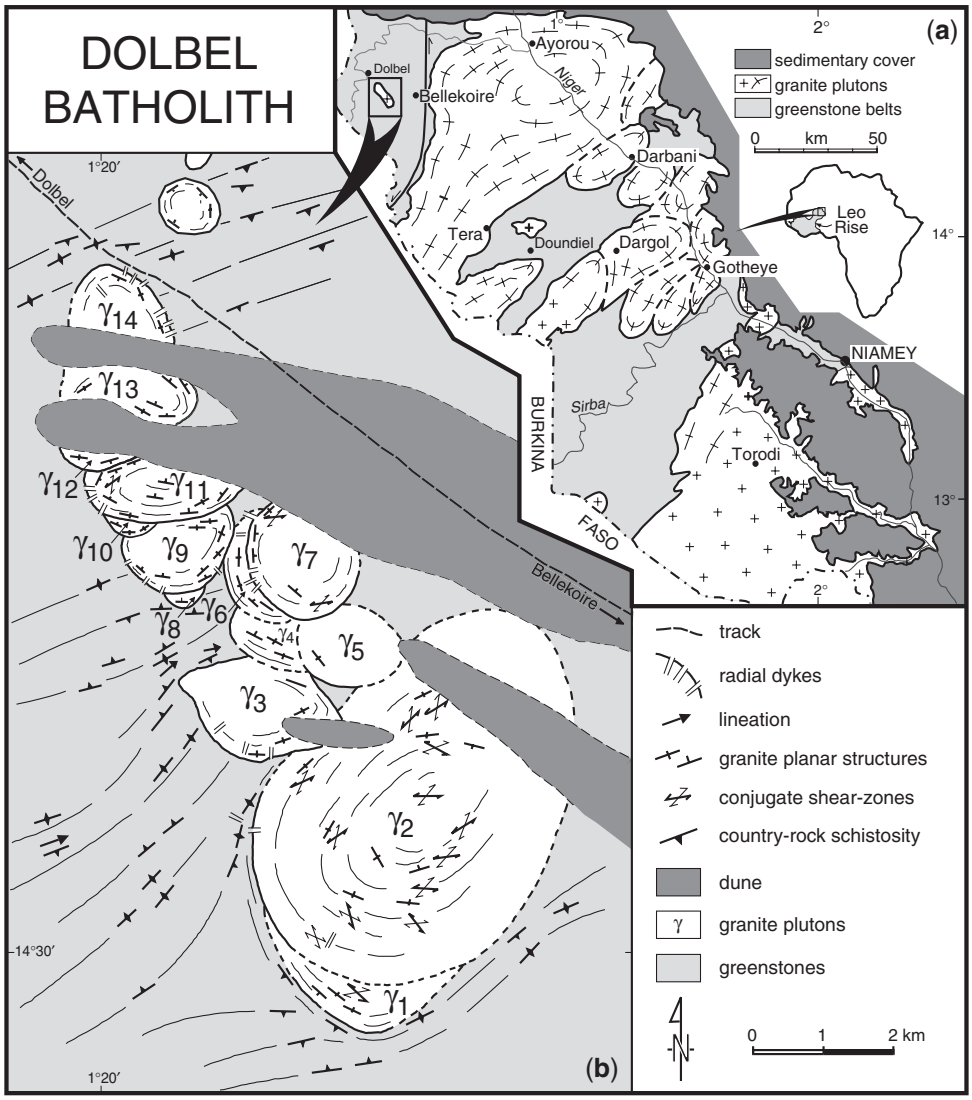

Fig. 1. Geological maps of (a) the Liptako area (SW Niger) and (b) the Dolbel batholith. Redrawn from Pons *et al.* (1995).

STRUCTURE AND ROCK TYPES OF THE DOLBEL PLUTONS

All plutons consist of low-Ca plagioclase ($An_{\leq 11}$), K-feldspar, quartz, amphibole, clinopyroxene and accessory minerals (principally titanite, apatite and magnetite). The proportions of ferromagnesian minerals average 5 vol. %, but may be locally significantly higher (≥20%). As shown by Pons *et al.* (1995), the plutons can be subdivided into two main parts: (1) a coarse-grained core consisting of granite showing only a weak fabric; (2) a peripheral layered series with a zone of high strain at the margin. The core of the plutons consists of porphyritic granite that contains sparse microgranular mafic enclaves (Fig. 2a), which may occur in swarms and correspond to proto-dykes. Locally, K-feldspar phenocrysts form irregular accumulations (Fig. 2b). These phenocrysts are generally of larger grain size than in the layered series, but display similar zoning patterns (Fig. 2c).

Structure of the plutons

The structure of the Dolbel plutons has been described by Pons *et al.* (1995) and only the principal characteristics are summarized here. In all plutons, the fabric is sub-vertical, sub-parallel to the igneous layering and parallel to the contact with the surrounding schists (cylindrical geometry). The fabric corresponds to a schistosity in the periphery of the plutons. It is particularly well expressed in the largest γ^2 pluton, close to the contact with the host-rocks, where the zone of high strain may exceed 10 m in thickness. Here the granite looks like an orthogneiss, with intense plastic deformation of minerals (elongated quartz grains,

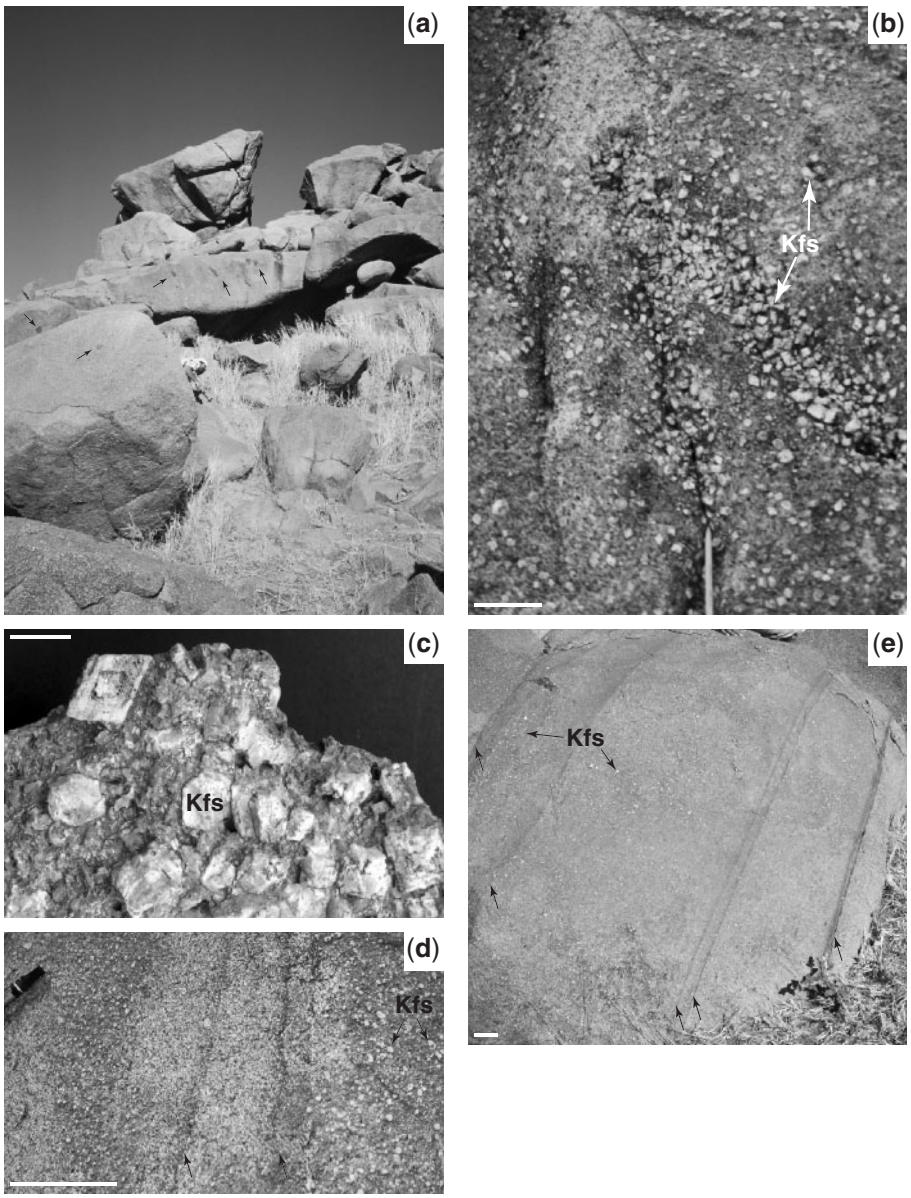

Fig. 2. Field photographs of the Dolbel γ^2 pluton. (a) Homogeneous porphyritic granite in the core, with sparse mafic microgranular enclaves (arrowed). (b) Local accumulation of K-feldspar phenocrysts in the core of the pluton. (c) Thin oscillatory zoning in K-feldspar outlined by weathering. (d) and (e) Sub-vertical, inward-dipping, igneous layering in the periphery of the intrusion showing dark amphibole-rich layers at the base and porphyritic granite at the top (pluton core located to the left). Arrows indicate amphibole-riche basal layers. Scale bar represents 10 cm, except in (c), where it represents 1 cm.

asymmetric recrystallized pressure shadows around rotated K-feldspar phenocrysts; see Pons *et al.*, 1995, fig. 7). In the rest of the pluton, the fabric, highlighted by the preferential orientation of amphibole and feldspars free of plastic deformation, can be defined as a 'pre-full crystallization fabric' (Hutton, 1988).

Shear zones are conspicuous in the periphery of the γ^2 pluton. Close to the contact, they deflect the schistosity sideways and are associated with intense plastic deformation, suggesting that they were produced during the late stages of pluton consolidation by ductile deformation of the outer shell of the pluton. Towards the pluton interior, shear zones, tens of centimetres long, are weakly defined by the orientation of plagioclase crystals (submagmatic deformation). They cut across the foliation without deflection or plastic deformation (see Pons *et al.*, 1995, fig. 8). The geometry of the shear zones (sub-vertical, concentric in conjugate or parallel sets, horizontal sense

of displacement) is systematic, where they occur. The conjugate shears make an angle of 50–60° and the acute bisector of the angle corresponds to the foliation or to the schistosity. The geometry of the conjugate shear zones, the directions of displacement and the general monoclinic symmetry of the fabric show the rotational nature of the deformation, with extension along the direction of strike of the schistosity and flattening perpendicular to the contact of the pluton. This, along with the elliptical shape of the γ^2 pluton and the deflection of the country rock schistosity (Fig. 1b), indicates interference between regional deformation and inflation of the pluton by the injection of magma in its centre. The parallel nature of the contact of the pluton, the layering, the submagmatic foliation and the subsolidus schistosity, together with the systematic geometry of the shear zones preclude any significant change in the dip of layering during the course of pluton growth.

The presence of vertical, radial dykes of aplite and quartz veins in the outermost parts of the plutons and in the nearby country rocks corroborates the existence of tensile stress concentric to the plutons, with flattening of the consolidated outermost shell (subsolidus deformation). Pons *et al.* (1995) considered that emplacement of the Dolbel plutons resulted from the interference between the regional strain field and a local strain field induced by inflation of the pluton caused by repeated inputs of fresh magma, which led to incremental finite strain in the outer part of the plutons.

The layered series

Data presented here and in the subsequent sections were obtained from the γ^2 pluton, unless otherwise stated. Layering corresponds to rhythmic variations in size, nature and proportions of minerals [the nomenclature used here is that of Irvine (1982)]. It is sub-vertical, dips steeply inwards (Fig. 2d and e) and is parallel to the contact of the pluton. Layering consists of rhythmic units that differ in width, although any single unit maintains a rather constant width along its strike at outcrop-scale. As a result of very discontinuous outcrop conditions, the thickness of the whole layered series is difficult to estimate, but exceeds several tens of metres. For the same reason, the sampled layering has been followed along its strike only over several tens of metres. The layering is described from one polished slab (Fig. 3), which is composed of four rhythmic cumulate units (C_1 to C_4). Mineralogical and geometrical characteristics of the four units are presented in Table 1. Of these four units, two are complete in terms of their mineralogical succession (C_3 and C_4), another is complete but was truncated when the sample was collected (C_1), and the fourth is incomplete (C_2) as it is missing its uppermost part. Taking the C_3 unit as a reference, a typical unit is considered to consist of three layers ($C_{a/p}$, C_q, C_k), each characterized by the appearance of a new cumulus mineral: amphibole/plagioclase, quartz and K-feldspar.

The lower, dark, $C_{a/p}$ layers show a sharp basal contact (Fig. 2d and e). At their base they consist almost exclusively of amphibole (+ apatite, titanite, Fe-oxide), whereas towards the top, both amphibole and plagioclase occur as cumulus phases. Plagioclase grains are low in abundance and of smaller size than in the subsequent layers. The C_q layers consist of cumulus plagioclase and quartz as the dominant minerals. In the C_k layers plagioclase, quartz and K-feldspar are cumulus phases. Size grading is particularly obvious for cumulus plagioclase and will be described in more detail below. A few clinopyroxene crystals also occur as a cumulus phase in the C_q and C_k layers. With the exception of quartz and clinopyroxene, all cumulus mineral phases are compositionally zoned, with remarkable oscillatory zoning. Intercumulus material consists mainly of quartz and K-feldspar, accompanied in lesser proportion by plagioclase and exceptionally by amphibole. Intercumulus minerals are not zoned, with the exception of a few intercumulus overgrowths. The proportion of intercumulus minerals (Table 1) is around 23–30% in the C_q and C_k layers, but negligible in the $C_{a/p}$ layers. Small mafic microgranular enclaves (millimetre to centimetre sized; Fig. 3) are scattered within the layered series. A few K-feldspar phenocrysts are locally present at the base of the rhythmic units.

Whole-rock compositions

Whole-rock analyses (see Appendix for analytical methods) of porphyritic granite from several pluton cores (Table 2) show major element compositions similar to those of sub-alkaline metaluminous granites, with $[Al_2O_3/(CaO+Na_2O+K_2O)]_{molar}$ ratios ranging from 0·79 to 0·95, and $[Al_2O_3/(Na_2O+K_2O)]_{molar}$ ratios ranging from 1·03 to 1·14. They are distinguished by their predominantly sodic compositions ($K_2O/Na_2O = 0{\cdot}49$–$0{\cdot}62$) and rather high $FeO_{tot}/(FeO_{tot}+MgO)$ ratios (0·65–0·82). Most trace element concentrations are low, including the rare earth elements ($\sum REE = 13{\cdot}6$–$42{\cdot}2$ ppm). Only Ba and Sr show high concentrations (averages: 2037 ± 463 and 1264 ± 340 ppm, respectively). Bulk major element compositions of the C_{2q}, C_{3q}, C_{1k} and C_{3k} layers are presented in Table 2. The C_k layers are not significantly different from the porphyritic granite samples, whereas the C_q layers differ by higher FeO_{tot}, MgO and REE contents but lower Al_2O_3, K_2O and Ba contents (650 ± 81 ppm). Bulk mineralogical proportions (wt %) of the $C_{a/p}$, C_q and C_k layers are given in Table 1.

REE patterns normalized to chondrite (Fig. 4) are similar in the samples from the core and the layered series. The REE are fractionated [$(La/Yb)_N = 4{\cdot}4$–$7{\cdot}0$], with concave-upward heavy REE [$(Gd/Yb)_N = 1{\cdot}5$–$2{\cdot}1$] and positive Eu anomalies ($Eu/Eu^* = 1{\cdot}1$–$1{\cdot}9$). The C_q samples show higher REE concentrations than the C_k layers and porphyritic granites, these higher values being probably related to higher proportions of titanite. It should be

Fig. 3. Polished slab of layered granite from the γ^2 pluton. The sample comprises four rhythmic units (C_1 to C_4); complete units consist of three successive layers: $C_{a/p}$ (amph + pl), C_q (amph + pl + qtz) and C_k (amph + pl + qtz + Kfs).

noted that the bulk REE contents in the Dolbel samples are significantly lower than those generally observed in A-type granites, which typically show chondrite-normalized Ce and Yb concentrations at least 100 and 30 times chondrite, respectively (e.g. Collins *et al.*, 1982).

MICROTEXTURES AND COMPOSITIONS OF MINERALS

Chemical compositions of minerals were determined by electron microprobe for major elements (*c.* 800 analyses) and by laser-ablation inductively coupled plasma mass spectrometry (ICP-MS) for trace elements (see Appendix for analytical procedures). Selected mineral compositions are presented in Table 3 (the complete dataset is provided as Supplementary Data available from http://www.petrology.oxfordjournals.org).

Ferromagnesian minerals

Clinopyroxene occurs as sparse euhedral crystals (0·2 × 0·6 mm to 0·4 × 2·0 mm) in the C_q and C_k layers. They are commonly surrounded by a thin rind of secondary actinolite, but in general they remain as small remnants partially replaced by an aggregate of secondary magnetite, epidote, K-feldspar and quartz. In the classification of

Table 1: Mineralogical composition and thickness of the C_a to C_k layers of the four rhythmic units (sample D90-18, γ^2 pluton)

Layer		Cumulus phases		Intercumulus
Name	Thickness (cm)	Main phases (wt %)	Subordinate phases (≤1%)	(vol. %)
Unit 4 (7·6 cm thick)				
C_{4k}	4·3 (incomplete)	plagioclase (64%), K-feldspar (8%), quartz (16%), amphibole (11%)	Cpx, Ox, Tit, Ap	27
C_{4q}	2·9	plagioclase (64%), K-feldspar (3%), quartz (18%), amphibole (15%)	Cpx, Ox, Tit, Ap	28
$C_{4a/p}$	0·4	amphibole (>80%), plagioclase (<20%)	Ox, Tit, Ap	—
Unit 3 (6·7 cm thick)				
C_{3k}	3·8	plagioclase (61%), K-feldspar (12%), quartz (13%), amphibole (12%)	Cpx, Ox, Tit, Ap	25
C_{3q}	2·6	plagioclase (54%), quartz (22%), amphibole (22%)	Cpx, Ox, Tit, Ap	27
$C_{3a/p}$	0·3	plagioclase (<20%), amphibole (>80%)	Ox, Tit, Ap	—
Unit 2 (1·4 cm thick)				
C_{2q}	1·0	plagioclase (54%), quartz (24%), amphibole (20%)	Cpx, Ox, Tit, Ap	25
$C_{2a/p}$	0·4	plagioclase (<20%), amphibole (>80%)	Ox, Tit, Ap	—
Unit 1 (4·6 cm thick)				
C_{1k}	4·6 (incomplete)	plagioclase (61%), K-feldspar (15%), quartz (12%), amphibole (10%)	Cpx, Ox, Tit, Ap	23

Intercumulus phases consist dominantly of quartz and K-feldspar.

Morimoto *et al.* (1988), the clinopyroxene corresponds to augite ($0{\cdot}65 < X_{Mg} < 0{\cdot}77$) close to the field of diopside ($0{\cdot}41 < X_{Wo} < 0{\cdot}46$) and with a limited acmite component ($0{\cdot}08 < X_{Ac} < 0{\cdot}12$).

Amphibole is a ubiquitous phase, although it is more abundant in the basal layer of each rhythmic unit ($C_{a/p}$). It occurs as clusters of euhedral grains ranging in size from $0{\cdot}05 \times 0{\cdot}12$ mm to $0{\cdot}7 \times 0{\cdot}8$ mm, and as inclusions in feldspars (locally in plagioclase laths, more generally in interstitial K-feldspar). It consists dominantly of dark green ferro-edenite and is commonly surrounded by a light green rim of secondary actinolite (Fig. 5a). In back-scattered electron images, ferro-edenite shows systematic oscillatory zoning, which is absent in actinolite. Zoning patterns allow three parts to be distinguished in the ferro-edenite portion: (1) a core showing disjointed zoning with crosscutting relationships and synneusis, suggesting transport, agglomeration, dissolution and overgrowth of the crystals (Fig. 5b); (2) an intermediate part in which thin oscillatory zoning is parallel to the growth faces of crystals (Fig. 5c and e); (3) intercumulus overgrowths showing a progressive compositional variation towards the rim (Fig. 5d). These textures are very similar to those reported in phenocrysts from certain dacitic lavas such as those from Unzen volcano (e.g. Sato *et al.*, 2005).

The composition of the primary zoned amphibole (Fig. 6a) encompasses the fields of ferropargasite, ferro-edenite and edenite ($0{\cdot}37 < X_{Mg} < 0{\cdot}55$). Secondary actinolite shows X_{Mg} values ranging from 0·49 to 0·68. Two main types of major element variations are observed in amphibole (excluding actinolite). The first is related to either oscillatory zoning or core–rim variations (Fig. 7a). A rimward decrease in X_{Mg} also occurs locally in intercumulus overgrowths (Fig. 6f). The second type of variation corresponds to an abrupt change at the top of the $C_{3a/p}$ layer, characterized by an increase in Fe^{2+}, Al_{tot} and K^+ and a decrease in Mg^{2+} and Ti^{4+} contents, when passing from the C_{1k}–$C_{3a/p}$ layers to the C_{3q}–C_{4k} layers (Fig. 6b–d). Otherwise, there is no systematic evolution of major element composition of amphibole from one layer or from one rhythmic unit to another.

Trace element concentrations were determined by laser-ablation ICP-MS (see Appendix for the analytical methods) on a zoned crystal from the $C_{2a/p}$ layer (analytical spots in Fig. 5e). Concentrations of Ba, Sr, Ti and V show the highest values in the core, with a decrease in the intermediate oscillatory-zoned part, and then a slight increase towards the rim (Fig. 7). Concentrations of Ce are low in the core, increase in the intermediate part, and then decrease in the rim. These variations are similar to those recorded in titanite (see below).

Plagioclase

Microtexture and composition

Plagioclase crystals show two distinct parts, irrespective of their position in the rhythmic units (Fig. 8a and b): (1) large cores with faint oscillatory zoning; (2) overgrowths of variable thickness (0·1–0·4 mm), part of which is clearly intercumulus. Crystals are commonly tiled (Fig. 8b). Locally, plagioclase may be indented by adjacent

Table 2: Major (wt %) and trace (ppm) element composition of homogeneous porphyritic granite samples from the core of four plutons of the Dolbel batholith, and of the C_{2q}, C_{3q}, C_{3k} and C_{1k} layers from the γ^2 pluton

	Pluton core				Layered series			
Sample:	D28	D17	D48	D41	C_{2q}	C_{3q}	C_{3k}	C_{1k}
SiO_2	66·60	69·02	71·32	69·17	69·15	68·95	68·64	68·89
Al_2O_3	14·86	14·73	14·89	14·43	12·54	12·67	14·86	15·24
FeO_{tot}	2·95	1·95	1·75	1·31	4·24	4·60	2·71	2·44
MnO	0·07	0·03	0·03	0·03	0·07	0·08	0·05	0·04
MgO	1·56	0·55	0·42	0·45	1·46	1·61	0·94	0·77
CaO	3·10	1·63	1·46	1·67	2·93	3·29	2·97	1·83
Na_2O	6·06	5·91	5·73	6·12	5·47	5·31	5·86	5·57
K_2O	2·97	3·17	3·32	3·86	1·27	1·41	2·63	3·06
TiO_2	0·27	0·18	0·14	0·09	0·44	0·47	0·29	0·27
P_2O_5	0·21	0·10	0·10	0·12	0·11	0·12	0·07	0·07
LOI	0·90	0·86	0·79	0·92	1·21	1·57	1·22	0·72
Total	99·56	98·13	99·94	98·17	98·89	100·07	100·24	98·90
Ba	1648	1920	1872	2708	592	707	1573	2122
Co	7	—	5	6	11	12	7	6
Cr	55	8	8	20	14	15	9	8
Ni	25	9	14	18	11	12	8	7
Rb	55	85	77	51	29	30	57	64
Sr	1316	1428	1540	773	1101	1310	1491	1465
V	44	39	29	14	83	94	56	45
Y	8	6	4	4	8	8	5	4
Zn	68	61	60	51	126	135	79	68
Zr	81	68	71	57	152	151	93	84
La	7·3	2·5	4·0	1·4	5·34	5·75	3·76	2·53
Ce	20·7	8·7	12·5	6·9	12·98	13·42	8·44	7·16
Nd	7·9	3·6	4·1	1·9	8·44	8·49	5·40	3·90
Sm	2·0	1·2	1·2	0·7	2·26	2·24	1·41	1·09
Eu	0·6	0·5	0·5	0·50	0·75	0·79	0·66	0·61
Gd	1·3	0·8	0·9	0·9	1·86	1·89	1·24	0·90
Dy	1·1	0·6	0·7	0·6	1·42	1·44	0·93	0·72
Er	0·7	0·4	0·4	0·3	0·76	0·75	0·50	0·38
Yb	0·7	0·4	0·4	0·4	0·74	0·74	0·50	0·39
Lu	0·1	0·1	0·1	0·1	0·11	0·12	0·07	0·06

FeO_{tot}, total iron as Fe^{2+}; LOI, loss on ignition; —, below detection limit.

crystals, with evidence of resorption by pressure-solution of the overgrowth and, to a lesser extent, of the core (Fig. 8a). Plagioclase composition is albitic with a low anorthite component ($An_{0–1}$, Fig. 9a). The anorthite content of the cores, though typically ~An_7, is variable because of oscillatory zoning and secondary alteration. In some cases, overgrowths show an increase in An content, which

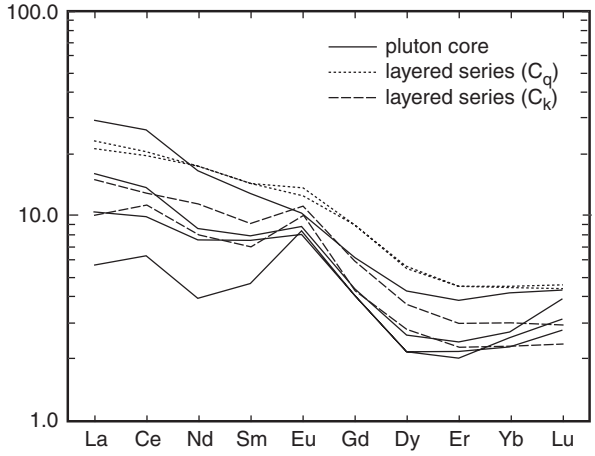

Fig. 4. Chondrite-normalized rare earth element patterns of porphyritic granites from pluton cores and of C_q and C_k layers from the layered series. Normalization values from Evensen *et al.* (1978).

then gradually decreases towards the contact with adjacent phases (Fig. 9b). Ba and Sr are the sole trace elements present in significant amounts in plagioclase (Fig. 10). Despite significant heterogeneity in core concentrations, Ba shows a systematic decrease in abundance towards crystal rims. Sr contents are even more heterogeneous, but display the same compositional trends as Ba. These compositional patterns are common to all plagioclases of the four units.

Crystal size distribution

In addition to geochemical observations, the crystal size distribution (CSD) may also provide insight into the high-temperature history of magmatic rocks (e.g. Marsh, 1998). The length, width, and area of plagioclase crystals were determined using NIH Image© software (see Pupier *et al.*, 2008). Lengths and widths are defined as the major and minor axes of the best-fitting ellipse of the two-dimensional crystal sections. In three dimensions, plagioclase shape can be considered as orthogonal, and defined by short (X), intermediate (Y) and long (Z) axes. For the case of orthogonal crystals, repeated measurement of the width of randomly chosen sections provides an estimate of the short axis X of the solid (Higgins, 1994, 2000). In the case of plagioclase, this represents the width perpendicular to {010}. Following Higgins (1994) [and as confirmed by Duchêne *et al.* (2008)], for each size class, the values of crystal number density measured in two dimensions [$N_a(L)$] were converted to values corresponding to a number density per unit volume $N_v(L)$ using the equation $N_v(L) = N_a(L)/(D \times 0{\cdot}64)$, where $N(L)$ is the total number of crystals whose size is smaller than L, and D is the mean size [$=(X+Y+Z)/3$]. For the calculation of D, X is considered as the midpoint of the interval ΔL, whereas Y and Z may be calculated from independent constraints on crystal shape (i.e. from known values of X/Y and Y/Z). Here an $X:Y:Z$ ratio of 1:2·22:4·75 has been used

Table 3: Selected mineral compositions from the C_3 rhythmic unit

Layer:	$C_{3a/p}$	$C_{3a/p}$	C_{3q}	C_{3q}	C_{3k}	C_{3q}	C_{3k}	$C_{3a/p}$
Mineral:	Ed	Act	Cpx	Plag	Kfs	Mgn	Tit	Ep
SiO_2	42·05	54·12	51·69	66·67	64·28	0·00	30·28	36·03
TiO_2	1·08	0·00	0·07		18·74	0·00	38·19	0·00
Al_2O_3	9·97	0·29	0·93	21·02		0·00	1·23	19·96
Cr_2O_3			0·01			0·01		
$Fe_2O_3^{tot}$							0·87	19·14
FeO^{tot}			12·70	0·15	0·00	93·00		
$Fe_2O_3^{calc}$	0·00	1·52	2·91			68·93		
FeO^{calc}	22·56	13·67	10·08			30·97		
MnO	0·36	0·58	0·41			0·02	0·08	0·14
MgO	7·84	14·97	9·86	0·02	0·02	0·00	0·02	0·03
CaO	9·92	12·52	21·77	1·54	0·00	–	28·03	21·77
Na_2O	2·29	0·19	1·27	10·54	0·28	–	0·02	–
K_2O	1·77	0·04	–	0·04	16·76	–	0·07	–
H_2O^{calc}	1·93	2·06					1·13	1·74
Total	99·78	99·95	99·01	99·98	100·08	99·93	99·92	98·82
Si	6·53	7·86	1·98	2·92	2·98	0·00	4·00	3·00
Al^{iv}	1·47	0·05	0·02					
Al^{vi}	0·35	0·00	0·02					
Al^{tot}				1·09	1·02	0·00	0·19	1·96
Ti	0·13	0·00	0·00			0·00	3·79	0·00
Fe^{3+}	0·00	0·17	0·13	0·00	0·00	2·00	0·08	1·08
Fe^{2+}	2·93	1·66	0·28			1·00		
Mn	0·05	0·07	0·01			0·00	0·01	0·01
Mg	1·81	3·24	0·56			0·00	0·00	0·00
Ca	1·65	1·95	0·90	0·07	0·00		3·97	1·94
Na	0·69	0·05	0·10	0·90	0·03		0·00	0·00
K	0·35	0·01		0·00	0·99		0·01	0·00
$\sum$ cations	15·95	15·06	4·00	4·98	5·02	3·00	12·05	7·99
O	23·0	23·0	6·0	8·0	8·0	4·0		12·5
$Mg/(Mg+Fe^{2+})$	0·38	0·66	0·67					
Ab				92·3	2·5			
An				7·4	0·0			
Or				0·2	97·5			

Ed, edenite; Act, actinolite; Cpx, clinopyroxene, Plag, plagioclase; Kfs, K-feldspar; Mgn, magnetite; Tit, titanite; Ep, epidote.

based upon a 3D reconstruction of sequentially polished sections of an experimental sample (Duchene *et al.*, 2008). We note in passing that the chosen values of X/Y and Y/Z have almost no effect on the relative CSDs determined in different layers, although the absolute position of the CSDs may be affected to some extent.

Plagioclase crystals are tabular, with average size increasing towards the top of each unit ($0{\cdot}2 \times 0{\cdot}6$ mm to $1{\cdot}7 \times 4{\cdot}3$ mm). Plagioclase CSD has been determined in each rhythmic unit. Measurements were made on euhedral plagioclase grains from all layers (avoiding intercumulus overgrowths) from thin sections cut perpendicular to the layering and planar fabric. The presence of a fabric is not an obstacle for measurements as it simply leads to X, Y and Z values closer to the true values. The number of measured grains ranges from 62 for the C_2 unit to 292 for the C_4 one. The data are available as Supplementary Data at http://www.petrology.oxfordjournals.org. CSD curves (Fig. 11) are similar in all the units and display a log–linear shape for large grain sizes. Slopes and intercepts of the regression lines in the different units are similar to each other, for both short and long axes of the crystals. Ratios of the area occupied by plagioclase relative to the whole surface area of each unit (measured perpendicular to the layering) are not significantly different (5·7, 4·4, 4·5 and 4·9 for C_1 to C_4 units, respectively), implying that modal proportions are the same in each layer. All these data are consistent with the suggestion that crystallization conditions were similar in all four units; that is, each rhythmic unit records the same broad thermal history. The small size of plagioclase grains at the base of each rhythmic unit is of note, as it suggests significant ΔT values between the top and the base of two consecutive units.

K-feldspar

K-feldspar is the characteristic phase at the top of the rhythmic units (C_k layers), but it is also present as rare isolated grains within other layers (e.g. C_{3q} layer in Fig. 3). The thickness of these C_k layers shows large variation: some are only a few centimetres thick whereas others are almost 1 m thick. C_k may even be absent, as in the incomplete C_2 unit. K-feldspar occurs as pink phenocrysts ($\sim 3 \times 4$ mm) which show a slight increase in size towards the top of each C_k layer ($\sim 5 \times 7$ mm), and as smaller anhedral intercumulus grains ($0{\cdot}06 \times 0{\cdot}08$ mm to $0{\cdot}2 \times 0{\cdot}3$ mm). Phenocrysts contain inclusions of euhedral to subhedral laths of plagioclase, euhedral edenite crystals and, in a few cases, subhedral, rounded quartz grains. The K-feldspar phenocrysts in the C_{1k}, C_{3k} and C_{4k} layers are homogeneously distributed. This may be appreciated from histograms of distance between K-feldspar phenocryst nearest neighbours (Fig. 12b), and is in contrast to what is observed in porphyritic granites from the pluton core, in which K-feldspar phenocrysts are unevenly distributed with local accumulations (Fig. 2b). K-feldspars have low albite component ($Or_{96–99}$, $Ab_{1–4}$; Fig. 12a), with the exception of a few perthites. Apart from the thin oscillatory zoning, there is an overall increase in Or and correlated decrease in Ab components towards grain edges (Fig. 12c). Back-scattered electron images (Fig. 8c and d) together with concentrations of Ba and Sr (Fig. 13) show that phenocrysts from all C_k layers consist of three

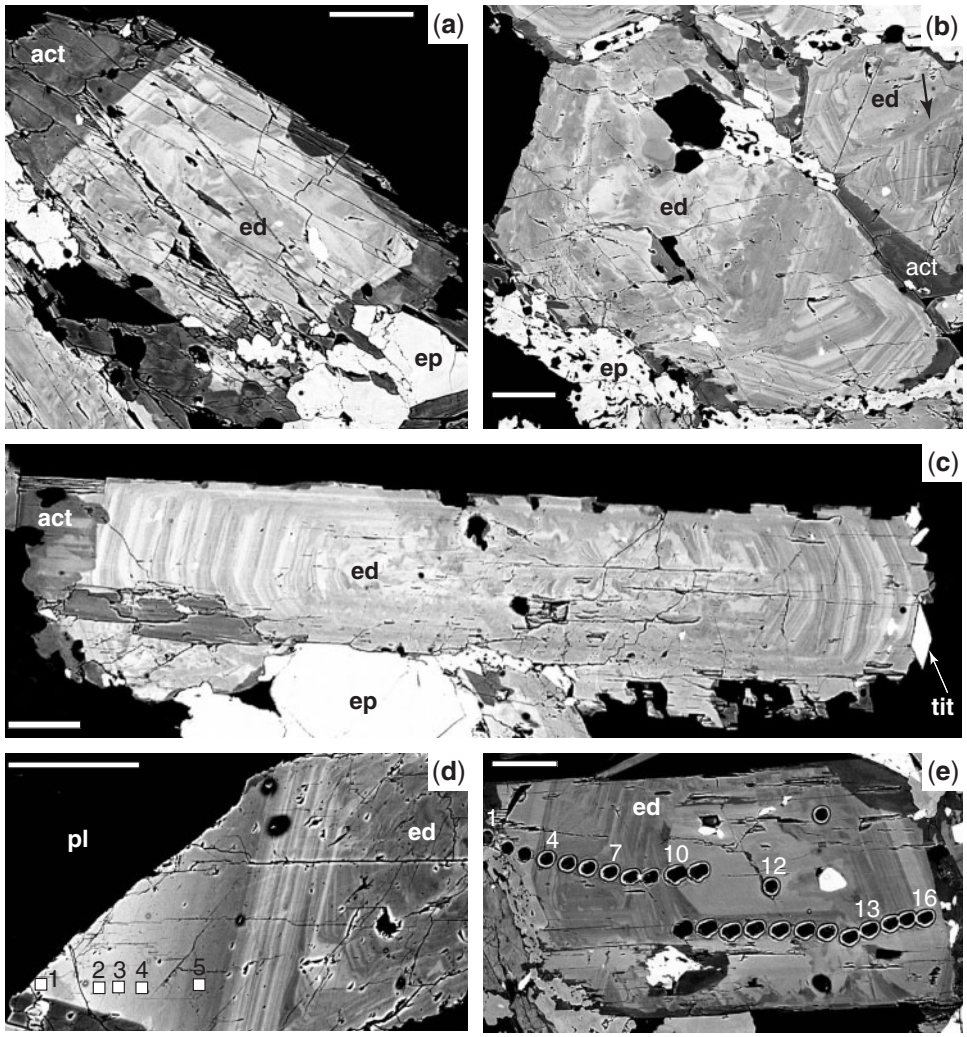

Fig. 5. Back-scattered electron images of amphiboles from the layered series (C_{2a} layer). (a) Oscillatory zoned ferro-edenite (light) partly replaced by actinolite (dark) at its periphery. (b) Ferro-edenites showing complex zoning in cores and regular euhedral zoning in the periphery; the presence of a synneusis microtexture should be noted (upper right, arrowed). (c) Euhedral lath-shaped edenite crystal showing patchy core, regular euhedral zoning and local retrogression into actinolite. (d) Intercumulus external part of an amphibole showing gradual change in composition (numbered filled squares refer to analyses of Fig. 6f). (e) Location of analytical spots in a zoned amphibole (numbers refer to Fig. 7). Scale bar represents 50 μm.

distinct parts. A perthitic core shows clear oscillatory zoning in Ba but at higher concentrations than the periphery and overgrowths. Apart from spikes related to the oscillatory zoning and secondary alteration, the variation of Ba concentrations show an overall concave-downward shape with decreasing values towards the rim. A euhedral periphery also shows oscillatory zoning, but is free of exsolution. It shows a significant decrease in Ba content. The external part corresponds to irregular overgrowths, dominantly as intercumulus material, enclosing all the other minerals. The Ba concentrations in these overgrowths are significantly lower than in the core and periphery. Sr is much more variable than Ba but shows the same trend, with a decrease in concentration towards the periphery of the crystals.

Microtexture and composition of other minerals

Quartz occurs as subhedral to euhedral, millimetre-sized, cumulus crystals in the C_q and C_k layers and as an ubiquitous intercumulus phase. Its size increases towards the top of each rhythmic unit, reaching 3 mm. No zoning was observed using cathodoluminescence microscopy.

Apatite, titanite and Fe–Ti-oxides are cumulus minerals associated with amphibole, especially in the basal $C_{a/p}$ layers. Apatite occurs as small euhedral zoned grains

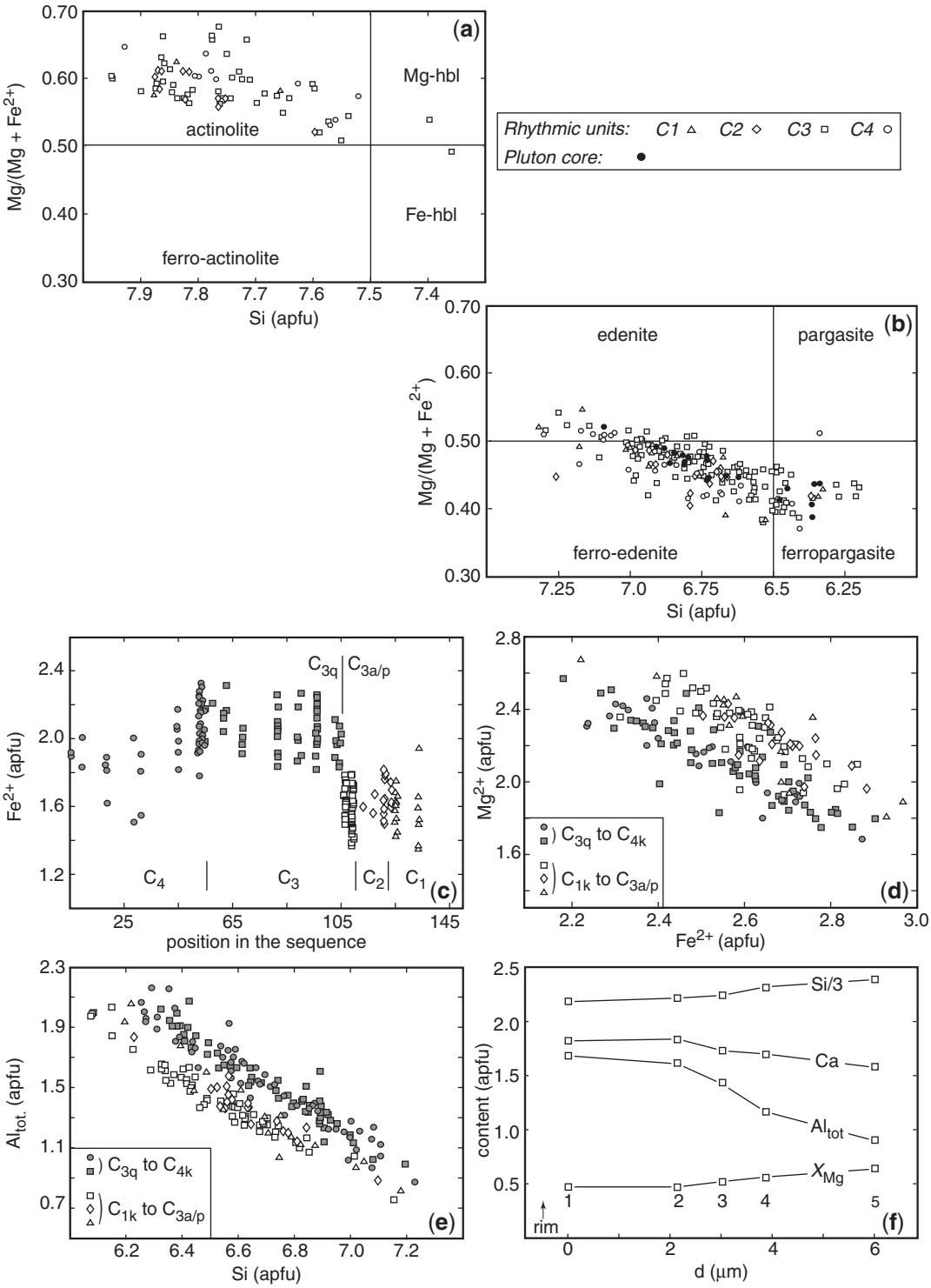

Fig. 6. Composition of the amphiboles from the layered series. (a) and (b) Amphibole compositions from the four rhythmic units plotted on the classification diagrams of Leake *et al.* (1997) showing that primary amphiboles consist mainly of ferro-edenite, whereas their overgrowths correspond to secondary actinolite. (c) Variations of Fe^{2+} content (atoms per formula unit) in ferro-edenite as a function of position in the rhythmic units (note the change just above the $C_{3a/p}$ layer). (d) and (e) Mg^{2+} vs Fe^{2+} and Al_{tot} vs Si plots also showing the abrupt change at the top of the $C_{3a/p}$ layer. (f) Variation in Al_{tot}, Si, Ca (a.p.f.u.) and X_{Mg} in the intercumulus overgrowth of Fig. 5d, showing a gradual decrease in X_{Mg} and Si towards the edge of the crystal and correlative increase in Al_{tot} and Ca.

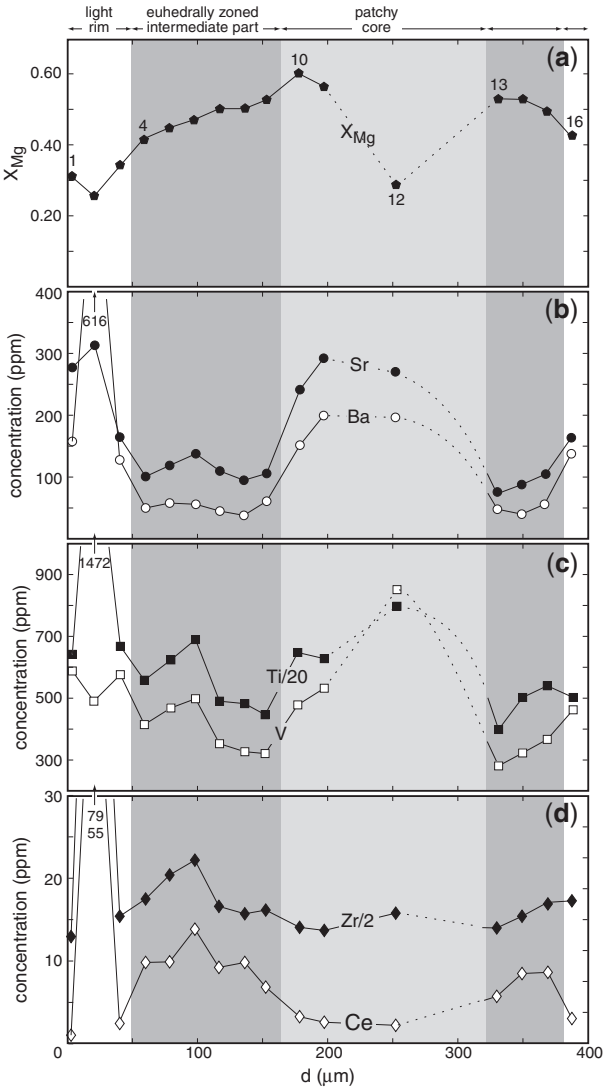

Fig. 7. Element variations in a ferro-edenite crystal (Fig. 5e): (a) X_{Mg}; (b) Ba and Sr; (c) Ti and V; and (d) Zr and Ce. Numbers in (a) refer to analytical spots.

(0·2 mm wide basal sections). Titanite occurs as euhedral grains (0·02 × 0·05 to 0·1 × 0·5 mm) containing quartz and ilmenite inclusions. Back-scattered electron images show complex zoning patterns, with resorption in the core and euhedral growth zones at the grain edges (Fig. 14a). Major and trace element compositions determined by laser-ablation ICP-MS across a zoned grain (Fig. 14e) show gradual depletion in Sr towards the rim, whereas V, Th, Y and REE have a more complex profile consistent with the variations of Al_2O_3, FeO and CaO. For instance, the concentrations in Al_2O_3, V, Th and $\sum$REE are relatively constant in the core, decrease across the intermediate zone, and then increase significantly in the wide periphery. These variations are reminiscent of that observed in amphibole (Fig. 7). Magnetite occurs as ovoid grains (0·2–1·0 mm in size) in all layers (Fig. 14b and d), and some grains have a thin rind that is enriched in Ti (Fig. 14c). It may be locally retrogressed to hematite. Ilmenite has been observed only as small inclusions (<50 μm) within titanite.

In addition to actinolite that replaces the periphery of edenite crystals, the main secondary phases are rare carbonate grains associated with amphibole, and pistachite occurring as small grains or as larger area of symplectite with quartz in $C_{a/p}$ layers.

DISCUSSION

Among the various mechanisms proposed to account for the formation of igneous layering in mafic bodies (see, e.g. Naslund & McBirney, 1996), two main processes are commonly invoked:

(1) hydrodynamic sorting related to density currents in magmatic suspensions, either by crystal segregation related to a velocity gradient along a static wall, or crystal settling related to material transfer towards the base of growing plutonic bodies (e.g. Barrière, 1981; Parsons & Becker, 1987; Tobisch *et al.*, 1997; Weinberg *et al.*, 2001; Wiebe *et al.*, 2002, 2007; Pons *et al.*, 2006);
(2) fractional crystallization in thermal boundary layers at the margin of magma chambers (e.g. Irvine, 1982; Irvine *et al.*, 1998).

Considering the near-vertical geometry of the layering in the γ^2 Dolbel pluton, and the absence of mineral grading, cross-stratification, trough layering and schlieren, crystal settling related to density currents can be ruled out. In the following sections we first discuss our data in the light of phase diagram constraints and then explore how the interplay of segregation in velocity gradients and fractional crystallization can explain the textural, mineralogical and chemical characteristics of the layered series.

Sequence and conditions of crystallization

The mineralogical, chemical and textural data described above provide numerous constraints on the physical and chemical processes that have led to the present-day layering. For example, the repetition of identical cumulate sequences from one rhythmic unit to another is interpreted to indicate that the parent melt for each unit was very similar. Given that whole-rock compositions are dominated by the four oxides SiO_2, Al_2O_3, Na_2O, and K_2O (their sum reaching 93% on average) and that plagioclase composition is close to pure albite ($An_{0–11}$) the Dolbel data may be satisfactorily represented and modelled in the Qz–Ab–Or haplogranite phase diagram. In light of this fact, it is immediately apparent that, excluding the basal amphibole-rich part of the $C_{a/p}$ layers, the principal changes in phase equilibria within a given unit are

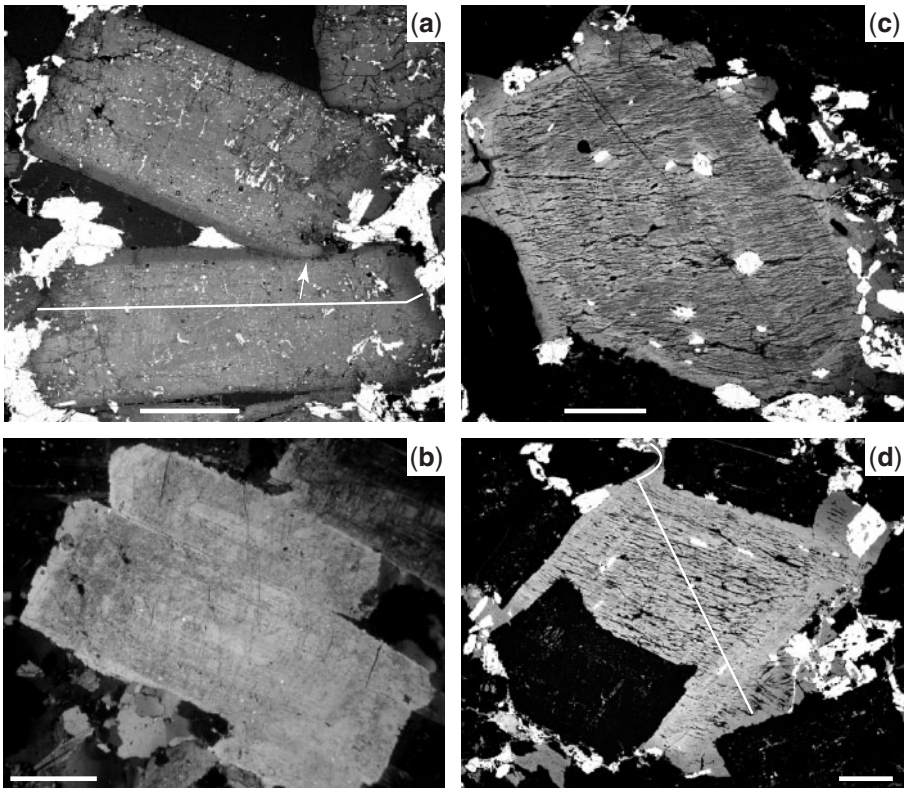

Fig. 8. Microtextures of feldspar from the layered series in back-scattered electron images. (a) Zoned plagioclase showing indented structure lacking the dark rim (arrowed); white line shows the location of the compositional profile shown in Fig. 9b (C_{1k} layer). (b) Tiled plagioclase crystals from the C_{1k} layer showing the rims (cross-polarized light image). (c) Ovoid K-feldspar phenocryst showing an oscillatory zoned core, a periphery and intercumulus overgrowths (C_{4q} layer). (d) K-feldspar phenocryst showing three parts: core, periphery and intercumulus overgrowths; the white line shows the position of the compositional profiles shown in Figs 12 and 13 (C_{3k} layer). Scale bar represents 0·5 mm.

consistent with an evolution involving liquidus (plagioclase in $C_{a/p}$), cotectic (plagioclase + quartz in C_q) and eutectic (plagioclase + quartz + K-feldspar in C_k) phase assemblages in the Qz–Ab–Or system (Fig. 15a), for parent melts located in the primary field of Albite. This is consistent with textural evidence showing that liquid saturation in K-feldspar occurred after amphibole, plagioclase and quartz. Furthermore, evidence for eutectic assemblages suggests pressure conditions of crystallization $\geq$5 kbar (Johannes & Holtz, 1996), in agreement with the metamorphic phase assemblages (kyanite + staurolite) reported by Pons *et al.* (1995) in the surrounding metasedimentary series, and with Al-in-hornblende barometry results (4·1 $\pm$1·4 kbar on average) determined from the Al_{tot} content of edenite using the calibration of Schmidt (1992).

Taking the C_3 rhythmic unit as a reference, we may assess to what extent the different cumulate layers represent successive instantaneous solid compositions resulting from fractional crystallization during cooling. If we discard amphibole, which will be discussed below, cumulus plagioclase from the $C_{3a/p}$ layer automatically has the composition of the liquidus phase assemblage. However, it is of note that the amount of plagioclase present in the $C_{a/p}$ layer is much lower than that expected based upon the phase diagram, assuming a parent liquid containing 20% normative quartz (see below). This low proportion of liquidus plagioclase may be the result of delayed or slow crystallization because of undercooling, as observed in experimental studies of plagioclase nucleation in basaltic compositions (Gibb, 1974; Walker *et al.*, 1976; Dowty, 1980; Tsuchiyama, 1983). The situation for silicic melts is less clear, although a theoretical study by Kirkpatrick (1983) suggested that crystallization may indeed be slow, a conclusion consistent with the sluggish crystallization kinetics of plagioclase observed experimentally by Couch (2003) in a haplogranite system.

Moving up-sequence, the bulk major element composition of the C_{3q} layer plots close to the Ab–Qz cotectic in the Qz–Ab–Or diagram (Fig. 15a). However, given the geometry of the phase diagram (Fig. 15), this observation does not necessarily imply that the layer C_{3q} has the composition of the original local liquid. This is because segregation and removal of eutectic melt interstitial to cotectic proportions of cumulus plagioclase and quartz results in

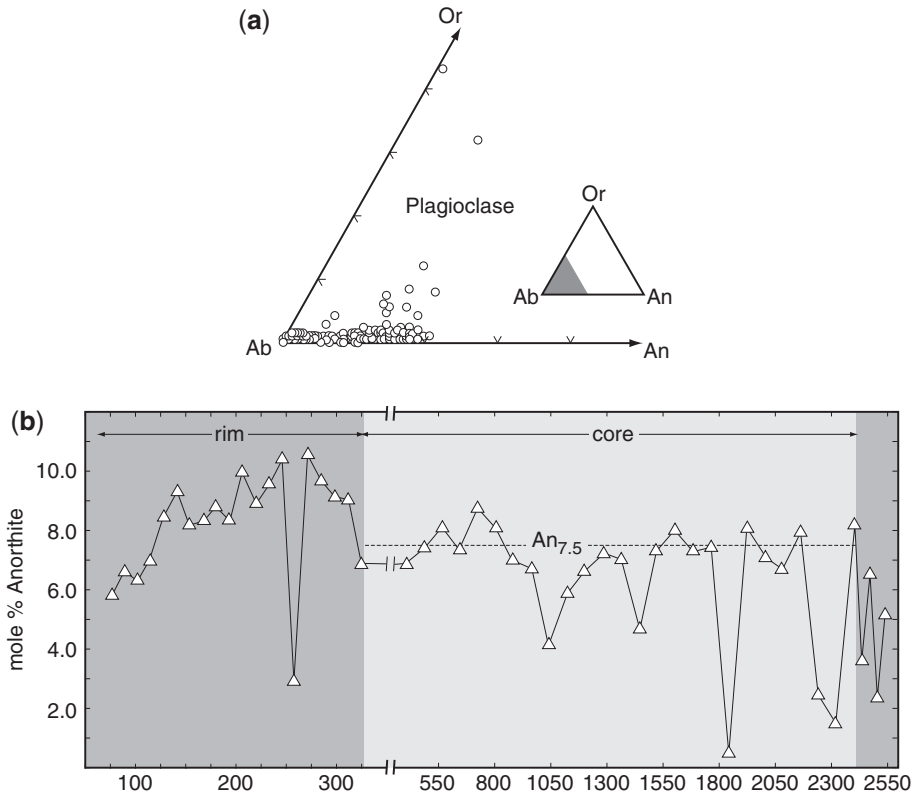

Fig. 9. (a) Composition of all the plagioclase crystals in the Ab–Or–An diagram showing the Na-rich composition of plagioclase. (b) Variation in anorthite (mol %) across the plagioclase crystal shown in Fig. 8a from the C_{1k} layer.

bulk compositions that appear to occur along the liquid cotectic. In other words, an unconstrained (but necessarily incomplete) fraction of interstitial eutectic liquid may have been removed from this layer during crystallization.

Moving to the uppermost layer of the sequence, we find that the composition of the C_{3k} layer is far from the eutectic and does not represent the crystallization product of the residual melt resulting from differentiation of the C_{3q} layer. It corresponds much more probably to the product of equilibrium crystallization of a melt close to the parent liquid composition (neglecting compaction-related removal of interstitial liquid). Indeed, the composition of this C_{3k} layer is not significantly different from the compositions of the granite samples from the core of the plutons. The differences correspond to locations either closer to the eutectic at $P_{H2O} = 10$ kbar (sample 2), or shifted toward the Or or Ab components (sample 4), or toward the 5 kbar eutectic (sample 3). Assuming that the parent melt composition was constant from one pluton to another, this may suggest that (1) parent melts might be close to eutectic liquids potentially formed at pressures around 10 kbar; and (2) that various proportions of eutectic residual melt were expelled from the cumulate, or local accumulation of feldspar occurred, in agreement with textural observations. If it is accepted that the bulk initial liquids were close in composition to the C_k layer, it would appear that, with the exception of edenite and accessory phases, the crystallization sequence was restricted to a small temperature interval (a few tens of degrees; see Fig. 15a and Scaillet *et al.*, 2000).

An alternative explanation for the observed mineral succession could be that it is the result of mechanical segregation in a velocity gradient along the wall of the magma chamber. Indeed, the fact that the size of K-feldspar phenocrysts is larger than that of both quartz and plagioclase, the latter being of comparable size, could be taken as evidence in favour of the mechanical segregation hypothesis. However, assuming that the C_{3k} layer has the composition of the initial melt composition, it may be appreciated from the Qz–Ab–Or diagram (Fig. 15), that mechanical subtraction of K-feldspar from the C_{3k} composition should lead to C_q layers located far below the cotectic curve. Moreover, there is no reason why mechanical segregation should lead to $C_{a/p}$ and C_q layers with almost identical thickness from one unit to another. Lastly, the zoning pattern of K-feldspar crystals implies closed-system conditions of growth (at least for the periphery and overgrowth) as shown by the strong decrease in Ba contents. In this respect, the distinct zoning patterns of K-feldspar cores (subhedral and regular) and edenite cores (disjointed, with textural

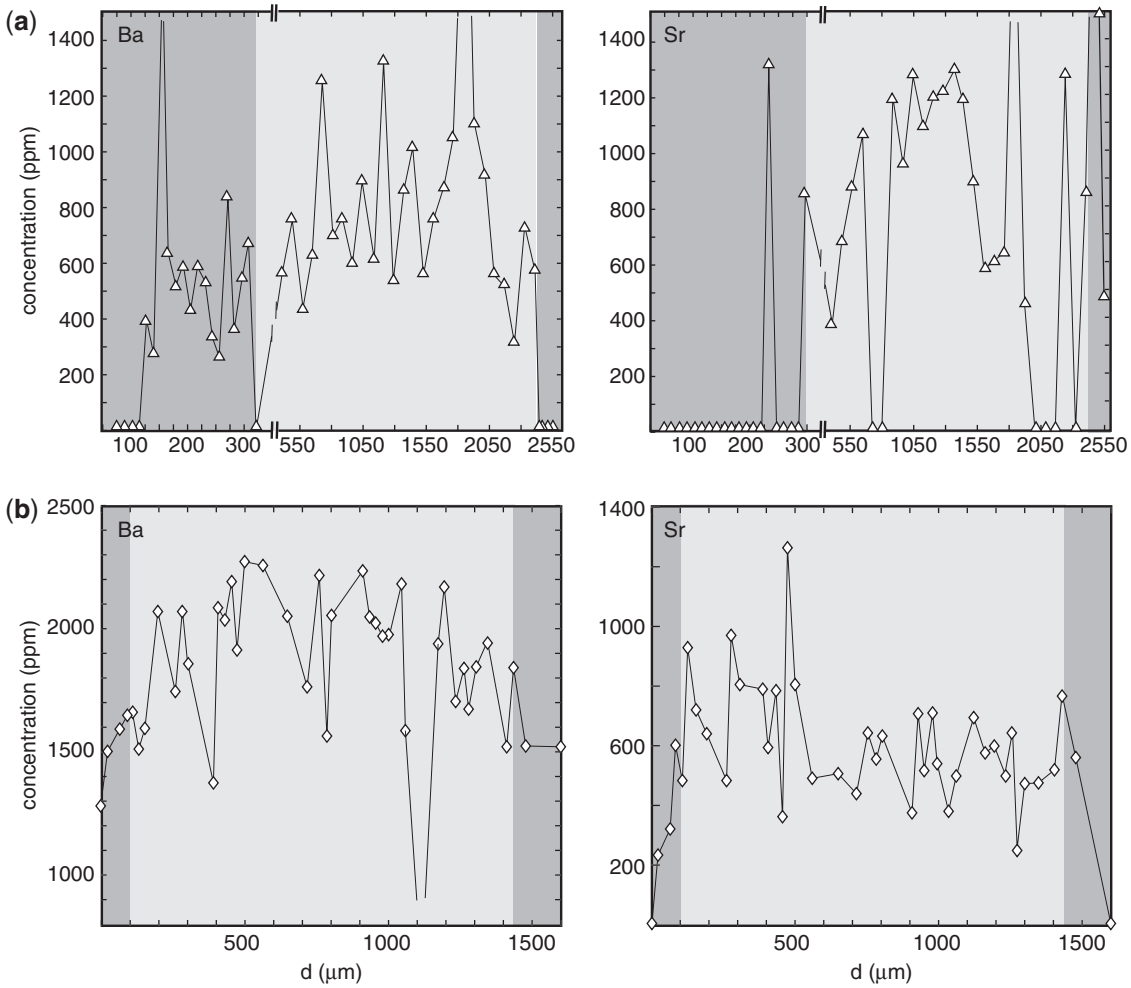

Fig. 10. Ba and Sr compositional profiles (ppm) in plagioclase crystals from (a) the C_{1k} and (b) the C_{2p} layers.

evidence of dissolution and regrowth) are striking, and argue against common conditions during their crystallization. In conclusion, we consider that hydrodynamic sorting does not account for the structures, textures and composition of feldspars and quartz.

The fact that edenite and other accessories (titanite, apatite and Fe–Ti oxides) are concentrated at the base of each rhythmic unit, and that they show cores with specific microtextures, suggests that they appeared early in the crystallization sequence. Experimental data at 3 kbar for compositions similar to that of the Dolbel granite (Dall'Agnol *et al.*, 1999) show that the liquidus temperature of amphibole in A-type granitic melts with 4–6 wt % H_2O is ~800–850°C (and up to 950°C in dacite; e.g. Prouteau & Scaillet, 2003; Holtz *et al.*, 2004), temperatures significantly higher than those expected for Na-rich plagioclase crystallization at 5 kbar from liquids close to the eutectic (<700°C). This raises the question of the origin of edenite and the accessory minerals: did they crystallize *in situ* or were they brought up with the magma to the site of emplacement? This will be dealt with in the next section.

A further point of note in the layered series is that amphibole crystallized before clinopyroxene, the latter occurring only as rare crystals in and above the C_q layers. Experimental data for metaluminous A-type granites at 3 kbar and reduced conditions (Dall'Agnol *et al.*, 1999) show that amphibole crystallizes before clinopyroxene at temperature around 800°C, and that for melt water contents of 4–5 wt % clinopyroxene starts to crystallize below 700°C. Moreover, X_{Fe} values of clinopyroxene (0·17–0·36) obtained in that experimental study may be higher than those of amphibole (0·20–0·71), and are comparable with the values found in the Dolbel granite samples (0·23–0·35 for clinopyroxene, 0·45–0·55 for edenite).

Finally, the overall stability of the magnetite + titanite + quartz assemblage in the Dolbel granites along with evidence for the presence of ilmenite preserved as inclusions in titanite suggest that variations in oxygen

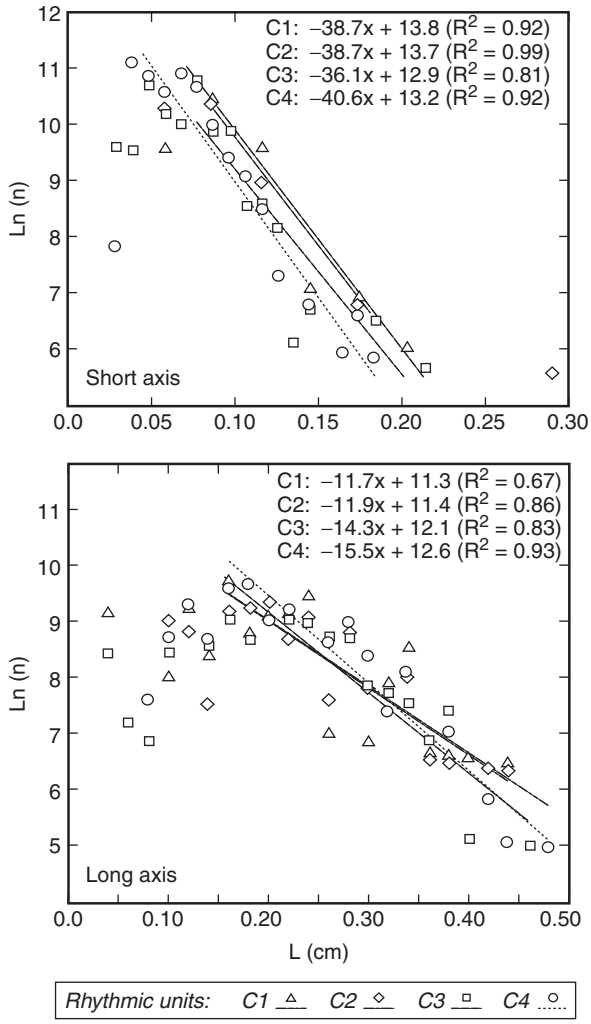

Fig. 11. Plots of the logarithm of the density of crystals ln (n) vs size class L, showing crystal size distribution curves for plagioclase short and long axes from the four rhythmic units. Slope, intercept and correlation coefficient are also indicated for the significant classes in each unit. The close parallelism of the CSD lines for the short axes should be noted.

fugacity occurred related to either cooling or to a change in redox conditions. The abrupt decrease in Fe^{3+} content in amphibole (and correlative increase in Al_{tot}) from the C_{3q} layer upwards would also support a change in fO_2 conditions under which edenite crystallized.

Significance of microtextures and chemical gradients in minerals

The systematic presence of very thin oscillatory zoning in amphibole, feldspars and titanite indicates that initial compositions related to crystallization are preserved. Retrogression of amphibole to actinolite (± epidote) is probably related to subsolidus hydrothermal transformation of limited extent such that the majority of magmatic amphibole is preserved. In the same way, alteration of both plagioclase and K-feldspar is limited to the presence of microporosity and of small white mica flakes. We can, therefore, consider that the variations in major and trace element concentrations are dominated by primary features that are related to crystal–melt partitioning during crystallization. Microtextures and chemical variations in amphibole, titanite and the feldspars allow four main stages to be distinguished during the development of a given layered sequence (Fig. 16).

Stage 1: crystallization in a convecting magma body

The first stage corresponds to the growth of edenite and titanite cores (the earliest phases to crystallize), which show complex zoning, with evidence of oscillatory growth, dissolution, overgrowth and grain aggregation (synneusis). Indeed, the cores of edenite crystals show the systematic presence of resorption surfaces, a feature commonly associated with changes in the physical conditions and/or melt composition caused by, for example, magma recharge (Nixon & Pearce, 1987; Ginibre *et al.*, 2002). X_{Mg} values are the highest in these parts of the crystals (Fig. 6a) and suggest crystallization from primary melts. All of these data along with the high liquidus temperature of amphibole and titanite imply the movement of early formed crystals within hot primitive liquids, inhibiting regular growth and leading to a complex succession of episodes involving dissolution and growth. Therefore, it is likely that the cores of both edenite and titanite did not crystallize *in situ* but formed in open systems (high liquid/crystal ratio) and were subsequently brought up with the magma to the site of emplacement (Fig. 16a). This raises the question of the nature of the basal amphibole-rich $C_{a/p}$ layers. Available data lead us to suggest that the edenite cores were mechanically aggregated by shear strain in a velocity gradient along the crystallized wall, whereas the external portions of the grains subsequently formed *in situ*.

Stage 2: crystallization in boundary layers

The second stage of crystallization is inferred to have occurred in a thermal boundary layer. This stage begins with the growth of the peripheral region of crystals of edenite and titanite and the crystallization of the plagioclase cores, as suggested by the common presence of thin and extremely regular oscillatory zoning mimicking euhedral crystal faces (Fig. 16b). The presence of this oscillatory zoning, attributed to kinetic effects at the crystal–liquid interface in multi-component systems (Allègre *et al.*, 1981; Putnis *et al.*, 1992), and the transition to this regime from the contorted and resorbed style of zoning observed in the cores of edenite and titanite clearly support a change from a dynamic to a calm physical environment between stages 1 and 2. Furthermore, in addition to textural arguments, geochemical variations also support the idea that the external zones of edenite and the cores of plagioclase

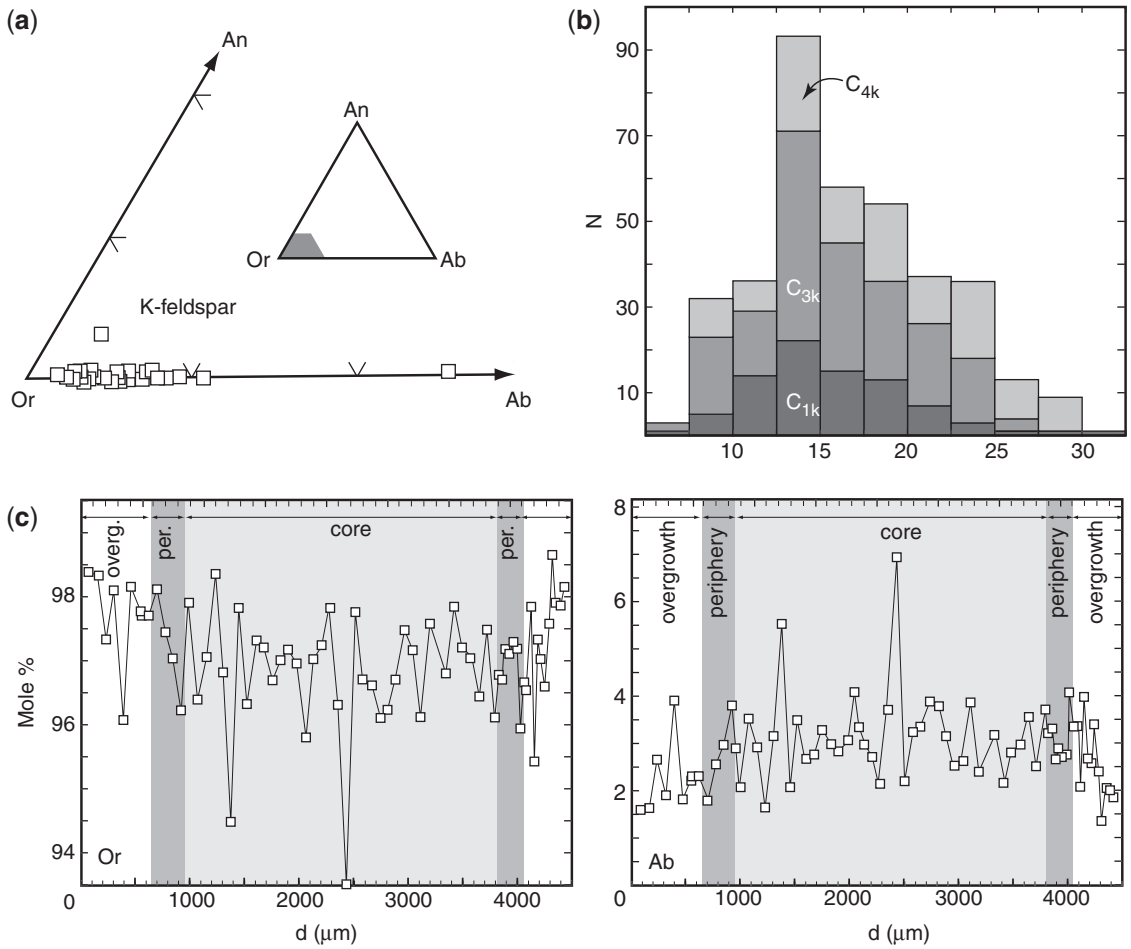

Fig. 12. (a) Composition of K-feldspar phenocrysts in the Or–An–Ab diagram. (b) Histogram of distances separating any K-feldspar phenocryst from its nearest neighbours, in the C_{1k}, C_{3k} and C_{4k} layers. (c) Or and Ab compositional profiles in K-feldspar phenocryst of Fig. 8d.

precipitated at the same time. For example, the external part of the core of edenite is characterized by a decrease in X_{Mg}, Ba, Sr, Ti, V and concomitant increase in Ce (Fig. 7), whereas the intermediate dark zone of titanite is characterized by a decrease in Al_2O_3, CaO and Sr with an associated increase in FeO and incompatible elements such as REE and Th (Fig. 14). Although the transition from the core to rim of titanite and edenite would appear to be concurrent with the onset of plagioclase crystallization, we cannot exclude the possibility that edenite started to grow *in situ* before plagioclase saturation occurred. On the other hand, the compositional variations recorded in both edenite and titanite imply that interstitial liquid was not renewed during this phase of crystal growth. This is a fundamental observation precluding the simple mechanical segregation of already grown crystals.

Quartz appears as a cumulus phase following plagioclase saturation (Fig. 16c). The fact that the bulk composition of the C_q layers is approximately cotectic may suggest that crystallization went to completion *in situ*, although, as noted above, the original bulk C_q compositions may have been closer to the eutectic, if a proportion of residual melt has been removed by compaction. However, the occurrence of interstitial K-feldspar together with quartz and plagioclase indicates that at least part of the residual melt remained trapped within the cumulate.

Stage 3: 'en masse' crystallization in closed system

The third stage of crystallization corresponds to the formation of the C_{3k} layer, in particular to the precipitation of K-feldspar phenocrysts and the growth of edenite rims (partly intercumulus) and the peripheral parts of plagioclase crystals (Fig. 16d and e). The existence of layers with bulk cotectic compositions suggests that plagioclase crystallized before K-feldspar, and this would appear to be supported by the fact that plagioclase may be found as inclusions within K-feldspar. However, the similarity in microtextures and trace element evolution in plagioclase and K-feldspar implies that K-feldspar crystallization did not significantly post-date plagioclase saturation.

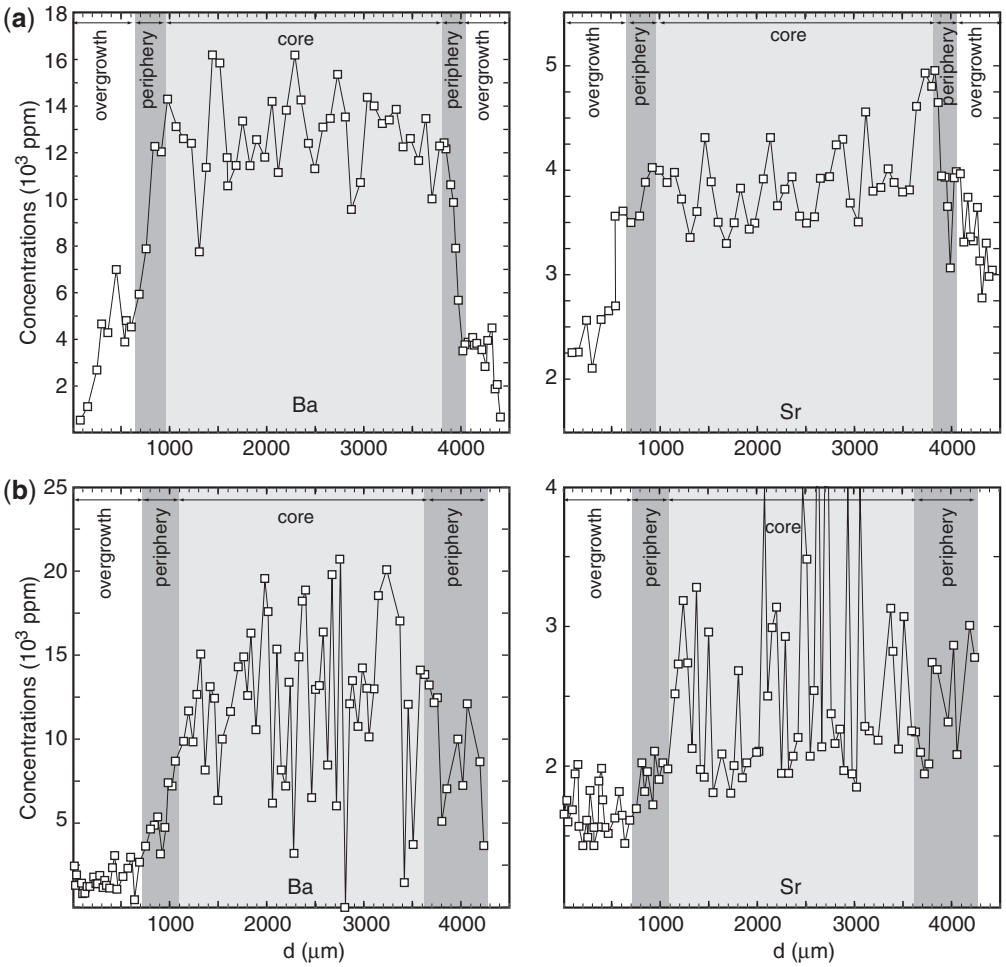

Fig. 13. Ba and Sr compositional profiles (ppm) in K-feldspar phenocrysts: (a) phenocryst from the C_{3k} layer (Fig. 8d); (b) phenocryst from the C_{1k} layer.

The rims to amphibole crystals show a decrease in X_{Mg}, whereas K-feldspars show an important decrease in Ba and Sr. Overgrowths of feldspars have very low Ba and Sr contents. These data indicate low liquid/crystal ratios and closed-system conditions for crystallization. The fact that the bulk composition of the C_{3k} layer remains far from the eutectic implies that during this stage there was no significant melt segregation, and that solidification occurred under conditions close to those of equilibrium crystallization. Textural relationships indicate that plagioclase and quartz were already in equilibrium with the melt before the onset of K-feldspar crystallization, whereas its occurrence as phenocrysts implies crystallization in a significant volume of melt. Moreover, phase relationships in the Qz–Ab–Or system at 5 kbar show that the temperature interval for cotectic and eutectic crystallization was restricted to about 20°C, if not less. This may, therefore, suggest that the bulk of the liquid crystallized at eutectic conditions by 'en masse' crystallization, with little or no removal of melt.

Stage 4: compaction and crystallization in the residual porosity

This last stage corresponds to compaction of the cumulate by the injection of a new magma batch (Fig. 16f). To a first approximation the volume of the intercumulus phases (measured to be 28% on average for the sample studied here) could correspond to the volume of residual melt left after inflation-related compaction. Assuming that before compaction occurred, a solid framework of melt fraction close to or lower than 50% existed for deformation to be efficient (the rigid percolation threshold; Vigneresse *et al.*, 1996), we estimate that less than 20% of the original intercumulus melt might be expelled by the compaction process. However, it should be noted that removal of this melt fraction cannot account for the low bulk REE contents (Fig. 4), if we consider that the REE patterns of A-type granites published by Collins *et al.* (1982) are representative of the parent melt of the Dolbel granites. This may suggest early fractionation of amphibole and titanite, in agreement with the fact that magmas were

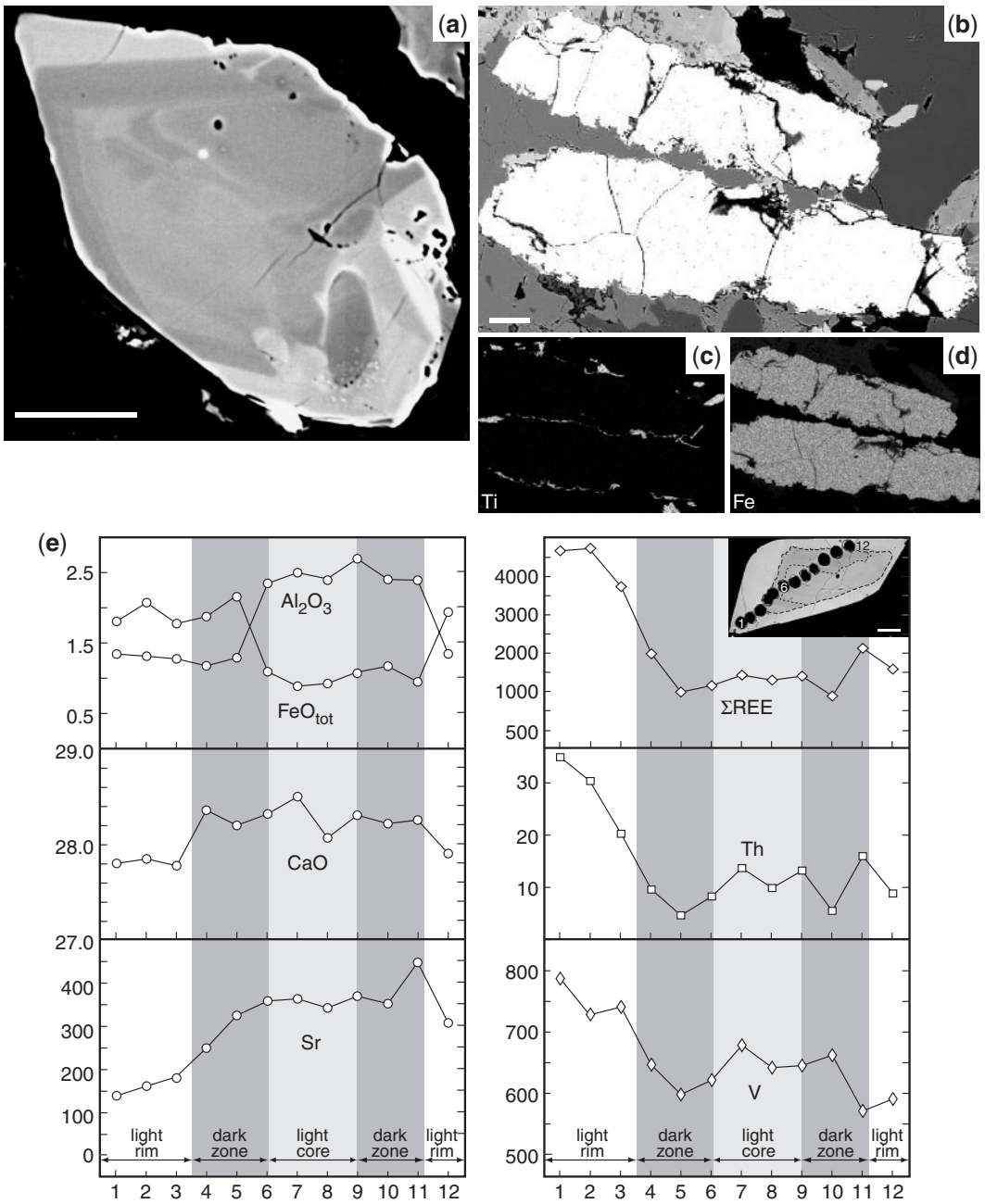

Fig. 14. Back-scattered electron images of accessory minerals. (a) Crystal of titanite showing a complex dark core partially resorbed and surrounded by a light rim (C_{1k} layer). (b) Magnetite grains from the C_{3k} layer. (c) and (d) X-ray images for Fe and Ti, respectively, of the same magnetite grains as in (b) showing the presence of small titanite grains around magnetite. (e) Compositional profile across a crystal of titanite from the C_{3a} layer (major elements: electron microprobe analyses in wt %; trace elements: laser-ablation ICP-MS analyses in ppm); inset: location of laser pits on the titanite. Scale bar in (a) and (b) represents 50 μm.

already saturated in these two phases when they arrived at the level of emplacement. Besides, some plagioclase crystals (e.g. Fig. 8a) show rims characterized by an increase in the An component followed by a subsequent decrease towards the contact. This reverse evolution of plagioclase composition suggests the percolation of a hotter, more primitive liquid through the framework of crystals, consistent with injection of a new magma batch, corresponding to the transition between stages 3 and 4.

The arrival of a new batch of magma will also result in the formation of a new rhythmic unit, with aggregation of small edenite crystals and incipient crystallization of

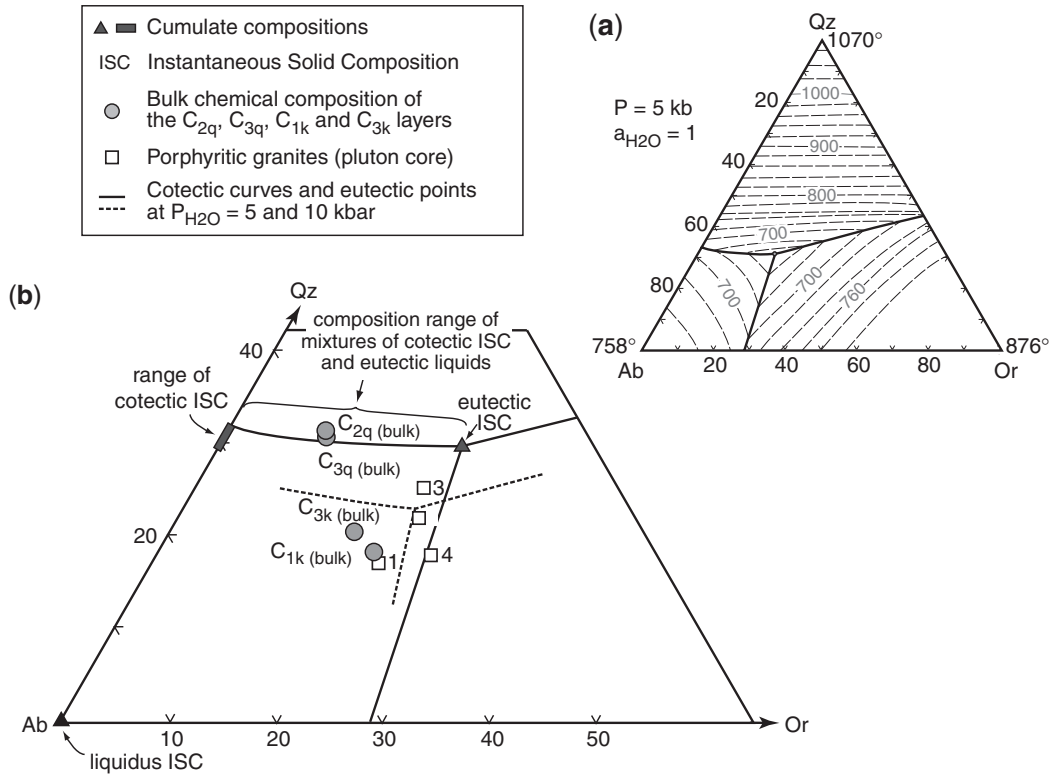

Fig. 15. (a) Qz–Ab–Or projection at $P_{H2O} = 5$ kbar from Johannes & Holtz (1996). (b) Plot of bulk compositions of the C_{1k}, C_{2q}, C_{3q} and C_{3k} layers and of porphyritic granites from the pluton core in the Qz–Ab–Or diagram at $P_{H2O} = 5$ kbar (also shown are the cotectic lines at 10 kbar).

plagioclase (Fig. 16g). Mechanical erosion induced by injection of a new batch of magma seems limited in most cases. However, the nature of the C_2 rhythmic unit, which is incomplete ($C_{2a/p}$ and C_{2q} layers only), shows that mechanical erosion may be important, perhaps because the C_3 liquid was emplaced when the C_2 unit still contained a high proportion of interstitial liquid and was more easily eroded away.

Implications for the magma emplacement process

The rhythmic layering in the Dolbel pluton

The repeated succession of the three layers forming each rhythmic unit and the compositional evolution of mineral phases can be interpreted simply in terms of fractional crystallization in boundary layers from a common parent magma, followed by 'en masse' equilibrium crystallization. Each rhythmic unit may correspond to arrival of a fresh magma batch and their repeated succession may represent crystallization of pulsed recharges as the magma body grew. This is corroborated by the plagioclase CSDs, which are identical from one unit to another, implying a similar thermal evolution for each unit. Moreover, the fact that cumulus plagioclase crystals in the $C_{a/p}$ layers, and quartz grains in the C_q layers are of smaller average size at the base of the relevant layer with a progressive increase in size towards the top suggests that nucleation is favoured with respect to growth at the base of each unit (higher values of supercooling). This is consistent with the emplacement of fresh magma batches at temperatures below the amphibole liquidus (i.e. $\leq$850°C) in contact with a eutectic mush (i.e. around 650°C). Nevertheless, there is no clear microtextural evidence of grain resorption. Accounting for the systematic cotectic composition of the C_q layers, for their constant thickness and for the zoning pattern of feldspars, the rhythmic units are unlikely to be formed only by crystal segregation in a velocity gradient in a crystal-laden magma flowing along a rigid wall. The variation in thickness for the C_k layers is a further important observation, which may be also rationalized in terms of the hypothesis that the growth of a rhythmic unit is arrested when a new magma batch is injected in the chamber, for temperature is raised or at least held constant by the new batch of magma. The variability in thickness of the C_k layers suggests that the frequency of injections was erratic (assuming a constant heat flux). In conclusion, we consider that the layered series of the γ^2 Dolbel pluton is an illustration of how fractional crystallization, flow segregation and the assembly of sequential magma injections interact.

Although the preservation of plagioclase CSD in each unit and the extremely homogeneous distribution of K-feldspar phenocrysts preclude hydrodynamic sorting,

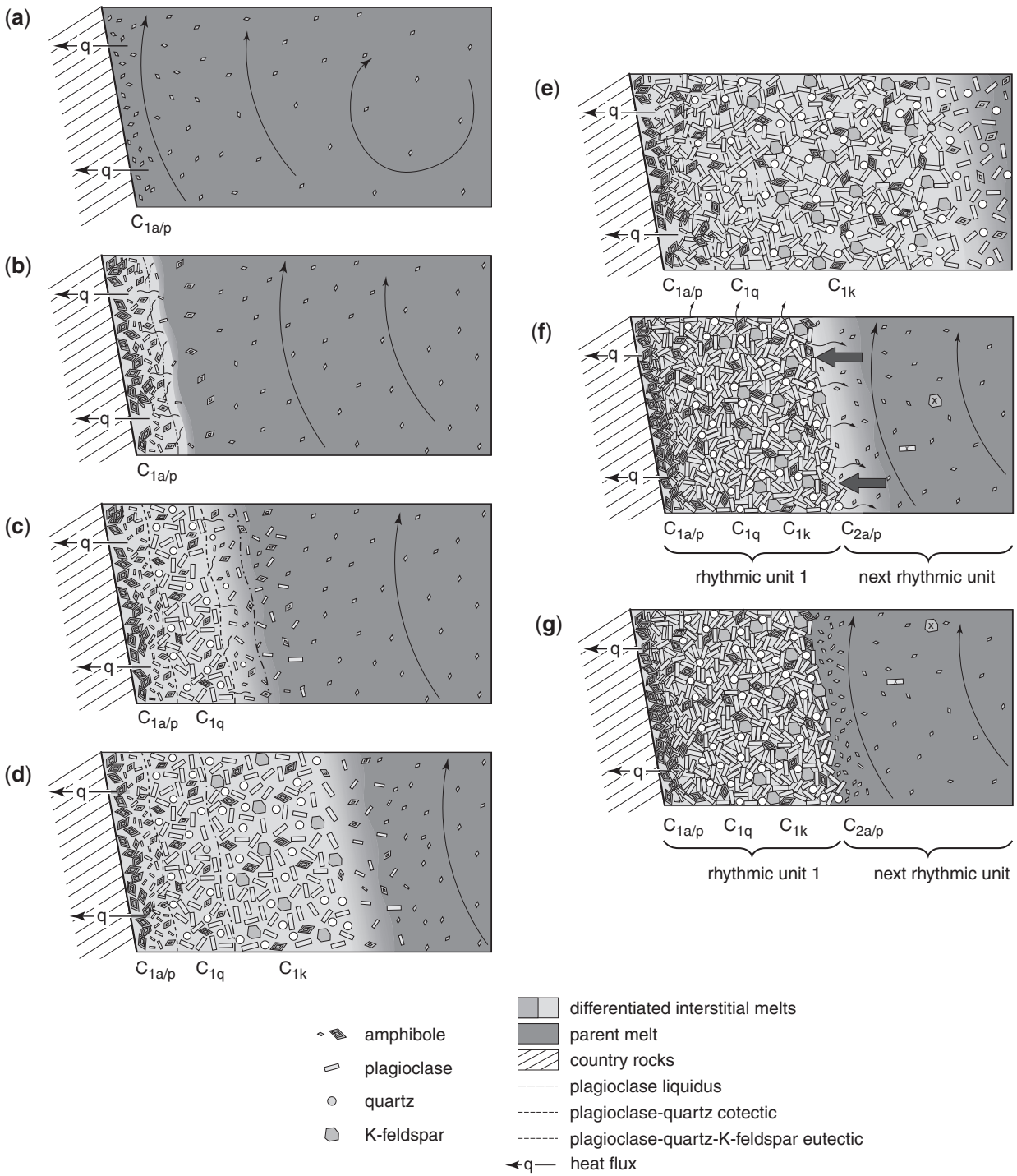

Fig. 16. Sketches illustrating the main formation stages of the rhythmic units (not to scale). Clinopyroxene and accessory phases are not represented. x, xenocrystic grains entrained in the melt. (a) Input of an amphibole-bearing and convecting magma batch, with aggregation of amphibole (core) along the wall. (b) Fractional crystallization under supercooling conditions, with plagioclase crystallization (core) and amphibole growth (periphery). (c) Fractional crystallization, with limited centimetre-scale melt movement, amphibole and plagioclase growth (periphery) and crystallization of quartz. (d) Equilibrium crystallization (no significant melt movement), with amphibole, plagioclase and quartz growth (periphery) and crystallization of K-feldspar. (e) Continued crystallization (no significant melt movement), with amphibole, plagioclase, quartz and K-feldspar growth ($F<0{\cdot}5$). (f) Input of a new magma batch inducing mechanical erosion and compaction (+ melt removal) of the former partially crystallized rhythmic unit. (g) Crystallization of the new magma batch starting with segregation of amphibole (core) along the wall, etc.

several observations suggest that the system was at least temporarily dynamic: (1) the textural characteristics of the edenite and titanite cores indicate that early flow segregation is likely to have occurred from magma batches already containing suspended crystals of edenite and accessory minerals; (2) the variable thickness of the C_k layers, including the absence of this layer in the C_2 unit, suggests mechanical erosion by new magma pulses; (3) the presence of rare K-feldspar phenocrysts outside the C_k layers indicates transport of suspended grains incorporated in the crystallizing unit, which could be derived from eroded C_k layers elsewhere in the pluton. Mobility of the melt, therefore, requires rather low viscosity values. We have estimated the viscosities of the parent melt between 650 and 850°C using the equation of Schulze *et al.* (1996) and the bulk composition of the C_{3k} layer. Considering melt water contents ranging from 5 wt % at 850°C (the amount of water required for amphibole to crystallize before clinopyroxene) to 10 wt % (saturation value at 650°C and 5 kbar; Johannes & Holtz, 1996) leads to liquid viscosities of $10^{4·2}$ to $10^{4·4}$ Pa s, values compatible with differential movement of melt and crystals.

The place and role of deformation

Pons *et al.* (1995) have shown that the deformation, characterized by a cylindrical geometry with concentric fabric and shear zones, is synchronous with the growth of the pluton and can be attributed to inflation caused by recurrent magma replenishment. In addition to a faint planar fabric and shear zones outlined by tiled plagioclase (see Pons *et al.*, 1995, fig. 8), deformation of the rhythmic units is also suggested by evidence of pressure dissolution at the grain scale. In the example shown in Fig. 8a, it is worth noting that dissolution of plagioclase post-dates the growth of its peripheral parts. Furthermore, we have seen that the periphery of K-feldspar phenocrysts corresponds to intercumulus overgrowths and that they have very low concentrations in Ba and Sr. This observation suggests that deformation-assisted compaction occurred after the growth of the periphery of plagioclase, but before crystallization of the intercumulus overgrowths. The proportion of intercumulus material in each rhythmic unit is estimated to be ~25%, suggesting that the intensity of deformation was limited, with removal of the interstitial melt and compaction of the mush only to the particle locking threshold of Vigneresse *et al.* (1996). On the whole, the similarity in proportions of intercumulus material and CSD curves in the four units suggests that each unit was compacted independently. If compaction were to have occurred once several rhythmic units were in place, then each unit would be expected to have a distinct amount of intercumulus material depending on how far crystallization had progressed in each layer, and this is not the case. The subsequent increments of deformation, related to injection of subsequent magma batches, led to limited subsolidus deformation (bent plagioclase twins, sub-grains in quartz), with the exception of the pluton periphery, where this deformation is much more pronounced (orthogneissification). An additional question implicit to deformation-assisted melt removal is how melt escaped the solid framework. There is no clear field evidence to determine whether interstitial melt has left through the intercumulus pore space or via channel structures such as the conjugate shear zones. Nevertheless, the radial dykes of aplite in the outermost zones of the plutons could represent such channels through which the residual melts escaped. Inflation-related compaction also accounts for the restricted nature of back reactions (growth of actinolite and epidote) and the absence of chemical re-equilibration in minerals during cooling, by removal of water-rich residual melts.

Significance of K-feldspar accumulations in the pluton core

K-feldspars may be unevenly distributed and form local accumulations in the core of the plutons (Fig. 2b). This observation contrasts with the very homogeneous distribution found in the layered series, which we interpret to be the result of *in situ* crystallization. This suggests that the presence of K-feldspar accumulation in the pluton core requires ssome additional process such as convection-related flow segregation. Whole-rock compositions of some granite samples from pluton cores (sample 4) appear shifted towards the Or end-member in the Qz–Ab–Or diagram (Fig. 15b). In conclusion, the distribution of mineral phases in the plutons, especially of K-feldspar phenocrysts, may be an indicator of mass transfer within the plutons (i.e. of convection).

CONCLUSION

This study shows that fractional crystallization in boundary layers (thermal and chemical gradients) is likely to occur in some granitic plutons, but remains limited to regions close to the wall-rock. Nevertheless, the bulk of the crystallization corresponds to 'en masse' eutectic-type crystallization. Flow segregation remains of limited extent, and is restricted to the early stage of growth of each rhythmic unit. The succession of rhythmic units is basically ascribed to recurrent injection of fresh magma batches, which then crystallize and differentiate *in situ*. This, therefore, fully corroborates the model of discontinuous magma input fed by a dyke (Clemens & Mawer, 1992; Vigneresse & Clemens, 2000). This also shows that granitic melt viscosities were low enough for differentiation and crystal–melt segregation to occur.

A further point raised by our study is to what extent the various rock units observed in silicic plutons may arise from *in situ* differentiation by fractional crystallization. We show that the C_k layers (i.e. the major part of the rhythmic units) result from the equilibrium crystallization of a parent magma close to a eutectic composition,

whereas only the $C_{a/p}$ and C_q layers are likely to result from fractional crystallization. Thus, the bulk of the melt solidifies by 'en masse' crystallization with little melt differentiation, as the magma locks up rapidly. This indicates that the large rock units occurring in most plutons, ranging in composition from gabbro to granite, are unlikely to result from *in situ* differentiation by fractional crystallization of unique parent magmas, as previously suggested (e.g. Cocherie *et al.*, 1994; Roberts *et al.*, 2000; Barbey *et al.*, 2001).

The Dolbel layered series probably represent an end-member situation in which fractional crystallization in a boundary layer and closed-system equilibrium crystallization associated with recharge are the dominant process during consolidation. At the opposite end of the spectrum, calc-alkaline plutons occurring commonly as mafic and silicic layered intrusions (Wiebe & Collins, 1998) probably represent another end-member situation in which the record of local crystallization processes has been largely wiped out by hydrodynamic processes related to episodes of mafic magma recharge (Pons *et al.*, 2006). Construction of a pluton is not a unique process simply involving intermittent magma input, but involves the combination of several processes, which may be more or less predominant depending on the context of emplacement and the magma composition. Therefore, the point is not to know whether fractional crystallization occurs or not in silicic magma bodies but, rather, to what extent it is blurred or impeded by other processes, especially those related to hydrodynamics. We suggest that there is not a unique process of construction of silicic plutons, but that there are various mechanisms (e.g. intermittent injection, convection, fractional crystallization, deformation), which may become predominant in specific parts of plutons at specific periods of time during pluton growth. This does not preclude, however, the existence of general trends for specific magma types, as for example in calc-alkaline plutons, where mafic replenishments and density currents appear to be the rule.

SUPPLEMENTARY DATA

Supplementary data for this paper can be found at *Journal of Petrology* online.

ACKNOWLEDGEMENTS

Thanks are due to J. Pons, who gave us the igneous layering sample from the Dolbel batholith, and to A. Kohler and J. Ravaux for assistance in scanning electron microscopy and electron microprobe analyses. We gratefully acknowledge the detailed review comments by F. Bea, E. W. Sawyer, R. A. Wiebe and by M. Wilson, the journal editor. This is CRPG Contribution 1917.

REFERENCES

Abouchami, W., Boher, M., Michard, A. & Albarède, F. (1990). A major 2·1 Ga event of mafic magmatism in West Africa: An early stage of crustal accretion. *Journal of Geophysical Research* **95**, 17605–17629.

Allègre, C. J., Provost, A. & Jaupart, C. (1981). Oscillatory zoning: a pathological case of crystal growth. *Nature* **294**, 223–228.

Aranguren, A., Larrea, F. J., Carracedo, M., Cuevas, J. & Tubia, J. M. (1997). The Los Pedroches batholith (southern Spain): polyphase interplay between shear zones in transtension and setting of granites. In: Bouchez, J. L., Hutton, D. H. W. & Stephens, W. E. (eds) *Granite: From Segregation of Melt to Emplacement Fabrics*. Dordrecht: Kluwer Academic, pp. 215–229.

Barbey, P., Nachit, H. & Pons, J. (2001). Magma-host interactions during differentiation and emplacement of a shallow-level, zoned granitic pluton (Tarçouate pluton, Morocco): implications for magma emplacement. *Lithos* **58**, 125–143.

Barrière, M. (1981). On curved laminae, graded layers, convection currents and dynamic crystal sorting in the Ploumanac'h (Brittany) subalkaline granite. *Contributions to Mineralogy and Petrology* **77**, 214–224.

Boher, M., Abouchami, W., Michard, A., Albarède, F. & Arndt, N. T. (1992). Crustal growth in West Africa at 2·1 Ga. *Journal of Geophysical Research* **97**, 345–369.

Boyce, J. W. & Hervig, R. L. (2008). Magmatic degassing histories from apatite volatile stratigraphy. *Geology* **36**, 63–66.

Carignan, J., Hild, P., Mévelle, G., Morel, J. & Yeghicheyan, D. (2001). Routine analyses of trace elements in geological samples using flow injection and low pressure on-line liquid chromatography coupled to ICP-MS: a study of reference materials BR, DR-N, UB-N, AN-G and GH. *Geostandards Newsletter* **25**, 187–198.

Cawthorn, R. G. (1996). *Layered Intrusions*. Amsterdam: Elsevier, 531 pp.

Clemens, J. D. & Mawer, C. K. (1992). Granitic magma transport by fracture propagation. *Tectonophysics* **204**, 339–360.

Clemens, J. D. & Petford, N. (1999). Granitic melt viscosity and silicic magma dynamics in contrasting tectonic setting. *Journal of the Geological Society, London* **156**, 1057–1060.

Cocherie, A., Rossi, Ph., Fouillac, A. M. & Vidal, Ph. (1994). Crust and mantle contribution to granite genesis. An example from the Variscan batholith of Corsica studied by trace element and Nd–Sr–O isotope systematics. *Chemical Geology* **115**, 173–211.

Coleman, D. S., Gray, W. & Glazner, A. F. (2004). Rethinking the emplacement and evolution of zoned plutons: Geochronologic evidence for incremental assembly of the Tuolumne Intrusive Suite, California. *Geology* **32**, 433–436.

Collins, W. J., Beams, S. D., White, A. J. R. & Chappell, B. W. (1982). Nature and origin of A-type granites with particular reference to Southeastern Australia. *Contributions to Mineralogy and Petrology* **80**, 189–200.

Couch, S. (2003). Experimental investigation of crystallization kinetics in a haplogranite system. *American Mineralogist* **88**, 1471–1485.

Dall'Agnol, R., Scaillet, B. & Pichavant, M. (1999). An experimental study of a lower Proterozoic A-type granite from the eastern Amazonian craton, Brazil. *Journal of Petrology* **40**, 1673–1698.

Dowty, E. (1980). Crystal growth and nucleation theory and the numerical simulation of igneous crystallization. In: Hargraves, R. B. (ed.) *Physics of Magmatic Processes*. Princeton, NJ: Princeton University Press, pp. 419–485.

Droop, G. T. R. (1987). A general equation for estimating Fe^{3+} concentrations in ferromagnesian silicates and oxides from microprobe

analyses, using stoichiometric criteria. *Mineralogical Magazine* **51**, 431–435.

Duchêne, S., Pupier, E., Le Carlier de Veslud, C. & Toplis, M. J. (2008). A 3D reconstruction of plagioclase crystals in a synthetic basalt. *American Mineralogist* (in press).

Evensen, N. M., Hamilton, M. J. & O'Nions, R. J. (1978). Rare-earth abundances in chondritic meteorites. *Geochimica et Cosmochimica Acta* **42**, 1199–1212.

Gibb, F. G. F. (1974). Supercooling and the crystallization of plagioclase from a basaltic magma. *Mineralogical Magazine* **39**, 641–653.

Ginibre, C., Kronz, A. & Wörner, G. (2002). High-resolution quantitative imaging of plagioclase composition using accumulated backscattered electron images: new constraints on oscillatory zoning. *Contributions to Mineralogy and Petrology* **142**, 436–448.

Glazner, A. F., Bartley, J. M., Coleman, D. S., Gray, W. & Taylor, R. Z. (2004). Are plutons assembled over millions of years by amalgamation from small magma chambers ? *GSA Today* **14**, 4–11.

Higgins, M. D. (1994). Numerical modelling of crystal shapes in thin sections: estimation of crystal habit and true size. *American Mineralogist* **79**, 113–119.

Higgins, M. D. (2000). Measurement of crystal size distribution. *American Mineralogist* **85**, 1105–1116.

Hodson, M. E. (1998). The origin of igneous layering in the Nunarsuit syenite, South Greenland. *Mineralogical Magazine* **62**, 9–27.

Holtz, F., Sato, H., Lewis, J., Behrens, H. & Nakada, S. (2004). Experimental petrology of the 1991–1995 Unzen dacite, Japan. Part I: Phase relations, phase composition and pre-eruptive conditions. *Journal of Petrology* **46**, 319–337.

Hunter, R. H. (1987). Textural equilibrium in layered igneous rocks. In: Parsons, I. (ed.) *Origins of Igneous Layering*. Dordrecht: D. Reidel, pp. 473–503.

Hutton, D. H. W. (1988). Granite emplacement mechanisms and tectonic controls: inference from deformation studies. *Transactions of the Royal Society of Edinburgh: Earth Sciences* **79**, 245–255.

Irvine, T. N. (1982). Terminology for layered intrusions. *Journal of Petrology* **23**, 127–162.

Irvine, T. N., Andersen, J. C. O. & Brooks, C. K. (1998). Included blocks (and blocks within blocks) in the Skaergaard intrusion: Geologic relations and the origins of rhythmic modally graded layers. *Geological Society of America Bulletin* **110**, 1398–1447.

Jang, Y. D. & Naslund, H. R. (2001). Major and trace element composition of Skaergaard plagioclase: Geochemical evidence for changes in magma dynamics during the final stage of crystallization of the Skaergaard intrusion. *Contributions to Mineralogy and Petrology* **140**, 441–457.

Johannes, W. & Holtz, F. (1996). *Petrogenesis and Experimental Petrology of Granitic Rocks*. Berlin: Springer, 335 pp.

Kirkpatrick, R. J. (1983). Theory of nucleation in silicate melts. *American Mineralogist* **68**, 66–77.

Leake, B. E., Woolley, A. R., Arps, C. E. S. *et al.* (1997). Nomenclature of amphiboles. Report of the Subcommittee on Amphiboles of the International Mineralogical Association Commission on New Minerals and Mineral Names. *European Journal of Mineralogy* **9**, 623–651.

Maaløe, S. (1976). Zoned plagioclase of the Skaergaard intrusion, East Greenland. *Journal of Petrology* **17**, 398–419.

Machens, E. (1967). *Notice explicative sur la carte géologique du Niger occidental. Carte géologique à 1/200 000ème*. Direction des Mines et de la Géologie, Niamey, Niger, 36 pp.

Markl, G. & White, C. (1999). Complex zoning between super-calcic pigeonite and augite from the Graveyard Point sill, Oregon: A record of the interplay between bulk and interstitial liquid fractionation. *Contributions to Mineralogy and Petrology* **137**, 170–183.

Marsh, B. D. (1998). On the interpretation of crystal size distributions in magmatic systems. *Journal of Petrology* **39**, 553–599.

McNulty, B. A., Tobisch, O. T., Cruden, A. R. & Gilder, S. (2000). Multistage emplacement of the Mount Given pluton, central Sierra Nevada batholith, California. *Geological Society of America Bulletin* **112**, 119–135.

Milési, J. P., Feybesse, J. L., Keita, F., Ledru, P., Dommanget, A., Ouedraogo, M. F., Marcoux, E., Prost, A. E., Vinchon, C., Sylvain, J. P., Johan, V., Tegyey, M., Calvey, J. Y. & Lagny, Ph. (1989). Les minéralisations aurifères de l'Afrique de l'Ouest. Leurs relations avec l'évolution lithostructurale au Protérozoïque inférieur. *Chronique des la Recherche Minière* **497**, 3–98.

Morimoto, N., Fabriès, J., Ferguson, A. K., Ginzburg, V., Ross, M., Seifert, S. A. & Zussman, J. (1988). Nomenclature of pyroxenes. *Bulletin de Minéralogie* **111**, 535–550.

Morse, S. A. (1980). *Basalts and Phase Diagrams*. New York: Springer, 493 pp.

Naslund, H. R. & McBirney, A. R. (1996). Mechanisms of formation of igneous layering. In: Cawthorn, R. G. (ed.) *Layered Intrusions*. Amsterdam: Elsevier, pp. 1–43.

Nixon, G. T. & Pearce, T. H. (1987). Laser-interferometry study of oscillatory zoning in plagioclase: the record of magma mixing and phenocryst recycling in calc-alkaline magma chambers, Iztaccihuatl volcano, Mexico. *American Mineralogist* **72**, 1144–1162.

Parsons, I. (ed.) (1987). *Origins of Igneous Layering. NATO ASI Series*, 666 pp.

Parsons, I. & Becker, S. (1987). Layering, compaction and post-magmatic processes in the Klokken intrusion. In: Parsons, I. (ed.) *Origins of Igneous Layering. NATO ASI Series*, pp. 29–92.

Petford, N., Cruden, A. R., McCaffrey, M. J. W. & Vigneresse, J. L. (2000). Granite magma formation, transport and emplacement in the Earth's crust. *Nature* **408**, 669–673.

Pons, J., Barbey, P., Dupuis, D. & Léger, J. M. (1995). Mechanism of pluton emplacement and structural evolution of a 2·1 Ga juvenile continental crust. The Birimian of Southwestern Niger. *Precambrian Research* **70**, 281–301.

Pons, J., Barbey, P., Nachit, H. & Burg, J.-P. (2006). Development of igneous layering during growth of pluton: The Tarçouate Laccolith (Morocco). *Tectonophysics* **413**, 271–286.

Pouchou, J. L. & Pichoir, F. (1991). Quantitative analysis of homogeneous or stratified microvolumes appying the model 'PAP'. In: Heinrich, K. F. J. & Newbury, D. E. (eds) *Electron Probe Quantitation*. New York: Plenum, pp. 31–75.

Prouteau, G. & Scaillet, B. (2003). Experimental constraints on the origin of the 1991 Pinatubo dacite. *Journal of Petrology* **44**, 2203–2241.

Pupier, E., Duchêne, S. & Toplis, M. J. (2008). Experimental quantification of plagioclase crystal size distribution during cooling of a basaltic liquid. *Contributions to Mineralogy and Petrology* **155**, 555–570.

Putnis, A., Fernandez-Diaz, L. & Prieto, M. (1992). Experimentally produced oscillatory zoning in the (Ba, Sr)SO_4 solid solution. *Nature* **358**, 743–745.

Roberts, M. P., Pin, C., Clemens, J. D. & Paquette, J. L. (2000). Petrogenesis of mafic and felsic plutonic rock associations: the calc-alkaline Quérigut complex, French Pyrenees. *Journal of Petrology* **41**, 809–844.

Sato, H., Holtz, F., Behrens, H., Botcharnikov, R. & Nakada, S. (2005). Experimental petrology of the 1991–1995 Unzen dacite, Japan. Part II: Cl/OH partitioning between hornblende and melt

and its implications for the origin of oscillatory zoning of hornblende phenocrysts. *Journal of Petrology* **46**, 339–354.

Scaillet, B., Behrens, H., Schulze, F. & Pichavant, M. (1996). Water contents of felsic melts: application to the rheological properties of granitic magmas. *Transactions of the Royal Society of Edinburgh: Earth Sciences* **87**, 57–64.

Scaillet, B., Holtz, F. & Pichavant, M. (1997). Rheological properties of granitic magmas in their crystallization range. In: Bouchez, J. L., Hutton, D. H. W. & Stephens, W. E. (eds) *Granite: From Segregation of Melt to Emplacement Fabrics*. Dordrecht: Kluwer Academic, pp. 11–29.

Scaillet, B., Holtz, F. & Pichavant, M. (1998). Phase equilibrium constraints on the viscosity of silicic magmas 1. Volcanic–plutonic comparison. *Journal of Geophysical Research* **103**, 27257–27266.

Scaillet, B., Whittington, A., Martel, C., Pichavant, M. & Holtz, F. (2000). Phase equilibrium constraints on the viscosity of silicic magmas II: implications for mafic–silicic mixing processes. *Transactions of the Royal Society of Edinburgh: Earth Sciences* **91**, 61–72.

Schmidt, M. W. (1992). Amphibole composition in tonalite as a function of pressure: an experimental calibration of the Al-in-hornblende barometer. *Contributions to Mineralogy and Petrology* **110**, 304–310.

Schulze, F., Behrens, H., Holtz, F., Roux, J. & Johannes, W. (1996). The influence of H_2O on the viscosity of a haplogranitic liquid. *American Mineralogist* **81**, 1155–1165.

Spera, F. J. & Bohrson, W. A. (2001). Energy-constrained open-system magmatic processes I: general model and energy-constrained assimilation and fractional crystallization (EC-AFC) formulation. *Journal of Petrology* **42**, 999–1018.

Tait, S. R. & Jaupart, C. (1996). The production of chemically stratified and adcumulate plutonic igneous rocks. *Mineralogical Magazine* **60**, 99–114.

Tegner, C. (1997). Iron in plagioclase as a monitor of the differentiation of the Skaergaard intrusion. *Contributions to Mineralogy and Petrology* **128**, 45–51.

Tobisch, O. T., McNulty, B. A. & Vernon, R. H. (1997). Microgranitoid enclave swarms in granitic plutons, central Sierra Nevada, California. *Lithos* **40**, 321–339.

Toplis, M. J., Brown, W. L. & Pupier, E. (2008). Plagioclase in the Skaergaard intrusion: Part 1: Core and rim compositions in the Layered Series. *Contributions to Mineralogy and Petrology* **155**, 329–340.

Tsuchiyama, A. (1983). Crystallization kinetics in the system $CaMgSi_2O_6$–$CaAl_2Si_2O_8$: the delay in nucleation of diopside and anorthite. *American Mineralogist* **68**, 687–698.

Vigneresse, J. L. & Clemens, J. D., 2000. Granitic magma ascent and emplacement: neither diapirism nor neutral buoyancy. In: Vendeville, B., Mart, Y., Vigneresse, J. L. (eds) *Slate, Shale and Igneous Diapirs in and around Europe. Geological Society of London, Special Publication* **174**, pp. 1–19.

Vigneresse, J. L., Barbey, P. & Cuney, M. (1996). Rheological transitions during partial melting and crystallisation with application to felsic magma segregation and transfer. *Journal of Petrology* **37**, 1579–1600.

Wager, L. R. & Brown, G. M. (1968). *Layered Igneous Rocks*. Edinburgh: Oliver & Boyd, 588 pp.

Walker, D., Kirkpatrick, R., Longhi, J. & Hays, J. F. (1976). Crystallization history and origin of lunar picritic basalt sample 12002: Phase-equilibria and cooling-rate studies. *Geological Society of America Bulletin* **87**, 646–656.

Weinberg, R. F., Sial, A. N. & Pessoa, R. R. (2001). Magma flow within the Tavares pluton, northeastern Brazil: compositional and thermal convection. *Geological Society of America Bulletin* **113**, 508–520.

Wiebe, R. A. & Collins, W. J. (1998). Depositional features and stratigraphic sections in granitic plutons: implications for the emplacement and crystallization of granitic magmas. *Journal of Structural Geology* **20**, 1273–1289.

Wiebe, R. A., Blair, K. D., Hawkins, D. P. & Sabine, C. P. (2002). Mafic injections, *in situ* hybridization, and crystal accumulation in the Pyramid Peak granite, California. *Geological Society of America Bulletin* **114**, 909–920.

Wiebe, R. A., Jellinek, M., Markley, M. J., Hawkins, D. P. & Snyder, D. (2007). Steep schlieren and associated enclaves in the Vinalhaven granite, Maine: possible indicators for granite rheology. *Contributions to Mineralogy and Petrology* **153**, 121–138.

Witt-Eickschen, G., Seck, H. A., Mezger, K., Eggins, S. M. & Altherr, R. (2003). Lithospheric mantle evolution beneath the Eifel (Germany): constraints from Sr–Nd–Pb isotopes and trace element abundances in spinel peridotite and pyroxenite xenoliths. *Journal of Petrology* **44**, 1077–1095.

Zak, J. & Paterson, S. R. (2005). Characteristics of internal contacts in the Tuolumne Batholith, central Sierra Nevada, California (USA): Implications for episodic emplacement and physical processes in a continental arc magma chamber. *Geological Society of America Bulletin* **113**, 976–995.

Zellmer, G. F., Blake, S., Vance, D., Hawkesworth, C. & Turner, S. (1999). Plagioclase residence times at two island arc volcanoes (Kameni Islands, Santorini, and Soufriere, St. Vincent) determined by Sr diffusion systematics. *Contributions to Mineralogy and Petrology* **136**, 345–357.

APPENDIX: ANALYTICAL METHODS

Whole-rock major and trace element concentrations were determined by inductively coupled plasma atomic emission spectrometry (ICP-AES) and ICP-MS (CRPG-CNRS, Nancy), respectively, using HNO_3 solutions prepared from fused glass. Sample preparation, analytical conditions and limits of detection have been described by Carignan *et al.* (2001). Analytical uncertainties are given as 2% for major elements, and as 5% or 10% for trace element concentrations (except REE) higher or lower than 20 ppm, respectively. Precision for REE is estimated at 5% when chondrite-normalized concentrations are >10 ppm and at 10% when they are lower.

Major element composition of minerals and Ba and Sr concentration profiles of feldspars were determined using a CAMECA SX-50 electron microprobe (Service Commun de Micro-analyse, Université Henri Poincaré, Nancy). Operating conditions were: (1) 10 nA sample current, 15 kV accelerating potential, counting times of 20 s and a beam diameter of 1 μm for major elements; (2) 100 nA, 15 kV, 20 s and beam diameter of 1 μm for Sr and Ba in feldspars. Calibration was made on a combination of silicates and oxides. Data reductions were performed using the PAP correction procedure (Pouchou & Pichoir, 1991). Ferric iron has been estimated according to

Leake *et al.* (1997) for amphibole and Droop (1987) for the others mineral phases.

Laser-ablation ICP-MS analyses (with pit size diameters of 10–40 μm) were performed on polished rock thin sections at the Institute of Mineralogy and Geochemistry, University of Lausanne. The measurements were acquired with a 193 nm Lambda Physik© Excimer laser (Geolas 200M system) coupled to a Perkin–Elmer 6100 DRC ICP-MS system. Laser settings were 27 kV and 10 Hz repetition rate, yielding a fluence of about 12 J/cm^2 on the ablation site. Helium was used as carrier gas (1·1 l/mn). We chose NIST612 glass as external standard, and Ca and Al as internal standards for amphibole and titanite, respectively (on the basis of electron microprobe measurements on the ablation pit sites). BCR2 basaltic glass was used as a monitor to check for reproducibility and accuracy of the system. Results were within ±10% of the values reported by Witt-Eickschen *et al.* (2003). Data reduction was done using LAMTRACE, a spreadsheet developed by S. E. Jackson (Macquarie University, Sydney).

Ion microprobe analyses were made on a Cameca IMS 3f ion microprobe (CRPG-CNRS, Nancy). A 10 kV O^- primary beam of 15–20 nA intensity was focused to a spot of 20 μm in diameter. Secondary ions were accelerated to 4500 eV and analysed at a mass resolution of ~500 with an energy filtering at −80 ± 10 V. The background, ^{30}Si, ^{86}Sr, ^{88}Sr, ^{137}Ba and ^{138}Ba were measured by peak switching, with counting times of 3 s on each peak. Successive measurements were cumulated for 15 min on each sample position. Secondary ion currents are normalized to Si, and secondary yields relative to Si determined on three standard glasses (NBS 614, BHVO, BCR2G) ranging in composition from 49·9 to 72·0 wt %. There is no observable variation of the relative secondary yields of Sr and Ba for these standards, implying that the calibration is not dependent on the chemical composition of silicate samples.